Arab J Geosci (2016) 9: 603
DOI 10.1007/s12517-016-2629-x

ORIGINAL PAPER

Late Ediacaran post-collisional A-type syenites with shoshonitic affinities, northern Arabian-Nubian Shield: a possible mantle-derived A-type magma

Hisham Gahlan[1,2] · **Mokhles Azer**[3] · **Paul Asimow**[4] · **Khaled Al-Kahtany**[1]

Received: 4 March 2016 / Accepted: 1 August 2016 / Published online: 19 August 2016

Abstract The Abu Rumeil syenitic rocks represent the inner ring dyke of the Katherina Ring complex, southern Sinai, Egypt. They are divided petrologically into two types, alkali feldspar syenite and quartz syenite. The mineralogy and geochemistry of the syenites indicate an alkaline nature with a shoshonitic affinity. Although rare mafic xenocrysts overgrown by primary K-feldspars and overlapping rare earth element (REE) patterns indicate some role for crustal contamination, the trace element chemistry shows a dominant mantle contribution. The geochronology and field relations imply that the Abu Rumeil syenites were emplaced in a post-collisional, within-plate tectonic setting, yet they express the enrichments in large-ion lithophile elements relative to high field strength elements generally characteristic of subduction influence. We suggest that this signature is inherited from partial melting of a lithospheric mantle source previously affected by subduction during assembly of the Arabian-Nubian Shield. Little evidence of the early evolution of the suite is preserved; there are no associated mafic rocks. We therefore restrict our attention to a petrogenetic model that can explain the relations among the observed felsic composition. The REE patterns of all samples are enriched in light REE and fractionated, but it is notable that there are small positive Eu anomalies in the alkali-feldspar syenites contrasting with small negative Eu anomalies in the quartz syenites. Positive Eu anomalies suggest a cumulate nature for the alkali-feldspar syenites; there are also breaks in the slopes of most variation trends between the alkali-feldspar syenites and the quartz syenites. The general trends in all major oxides and trace elements within the suite can be modeled by fractional crystallization of feldspars—with smaller roles for pyroxene, biotite, apatite, and Fe-Ti oxides—from an intermediate liquid to form the quartz syenites and by assimilation of the near-liquidus phases into the same starting liquid to form the alkali feldspar syenites. The geothermobarometry of pyroxenes and amphiboles suggests shallow emplacement (<10 km depth) and crystallization temperatures ranging from 1100 °C down to 800 °C.

Keywords Sinai · Syenite · Post-collision · Shoshonite · Within-plate

Introduction

The Arabian-Nubian Shield (ANS) is one of the largest tracts of juvenile continental crust of Neoproterozoic age on Earth (Patchett and Chase 2002). It evolved as the northern segment of the East African Orogen, which formed in Neoproterozoic time through three main phases referred to as pre-collisional, collisional and post-collisional (Stern 1994, 2002; Patchett and Chase 2002; Stoeser and Frost 2006; Eyal et al. 2010; Be'eri-Shlevin et al. 2009, 2011). The pre-collisional phase (~820–700 Ma) comprises metamorphosed volcano-sedimentary rocks, ophiolite suites, and calc-alkaline metagabbro-diorite-granitoid rocks. The collisional phase (670–630 Ma) is characterized by an abundance of weakly

✉ Hisham Gahlan
hjhlan@yahoo.com

[1] Department of Geology and Geophysics, King Saud University, Riyadh 11451, Saudi Arabia

[2] Geology Department, Faculty of Science, Assiut University, Assiut 71516, Egypt

[3] Geological Sciences Department, National Research Centre, Dokki, Cairo 12622, Egypt

[4] Division of Geological and Planetary Sciences, California Institute of Technology, Pasadena,, CA, USA

deformed calc-alkaline gabbros and granodiorites. The post-collisional phase (~620–580 Ma) is widely distributed in the northern part of the ANS and characterized by vast intrusions of calc-alkaline and alkaline/peralkaline granitoids and their associated volcanics. The ANS was stabilized before the development of an extensive peneplain in mid-Cambrian time (~530 Ma) and then exhumed in the Neogene due to Red Sea rifting and flank uplift (Garfunkel 1999).

Post-collisional A-type rocks in southern Sinai comprise dominant granites with lesser syenitic rocks. Previous studies on A-type igneous suites in southern Sinai have often focused only on granites. However, many types of granite classified as A-type are very similar chemically to highly fractionated I-type calc-alkaline granites associated with post-orogenic igneous suites (Bonin 2007; Eyal et al. 2010). Indeed, previous studies on Sinai granites reveal a large overlap between calc-alkaline and alkaline granites in many standard classification diagrams (Litvinovsky et al. 2015). Consequently, studies in southern Sinai based on granites may include misclassified samples and are likely to yield ambiguous answers about the distinctive processes associated with A-type magmatism.

The current contribution aims to define the petrogenesis of the Abu Rumeil syenites, distinctively alkaline members of the A-type igneous suite of the northern ANS (Sinai Peninsula, Egypt). New field, petrographical, geochemical, and mineralogical data are integrated to determine the petrological characteristics and history of the Abu Rumeil syenites. By constraining the source contributions to the magma and the processes and conditions of magmatic evolution, we can better understand the prevailing type of magmatism in the northern ANS (southern Sinai) during the Late Ediacaran, propose a tectonic and geochemical model for their origin, and evaluate their possible significance.

Geological background

The basement rocks of Sinai are the northernmost outcrops of the ANS. They are characterized by abundant post-collisional plutonic and volcanic sequences intruding and overlying older metamorphosed complexes. The post-collisional phase includes both calc-alkaline (ca. 635–590 Ma) and alkaline (ca. 610–580 Ma) plutonic suites and associated volcano-sedimentary sequences (Ali et al. 2009; Be'eri-Shlevin et al. 2009; Azer and El-Gharbawy 2011). There is an overlap between the end of calc-alkaline magmatism and the beginning of alkaline activity (Be'eri-Shlevin et al. 2009, 2011; Azer et al. 2010; Eyal et al. 2010). The post-collisional alkaline phase include A-type igneous rocks and is represented by alkaline volcanics, granites, ring complexes, and dyke swarms (Mushkin et al. 2003; Katzir et al. 2007; Samuel et al. 2007; Farahat and Azer 2011).

Ring complexes of Neoproterozoic age in many parts of the ANS (e.g., Harris 1985; Vail 1989; Katzir et al. 2007; Moghazi et al. 2011) were emplaced during the post-collisional phase of the shield (610–590 Ma). In the southern Sinai Peninsula in particular, the ring complexes are of late Ediacaran age (605–580 Ma; Katzir et al. 2007; Moreno et al. 2012, 2014; Eyal et al. 2014, Azer et al. 2014). The Katherina Ring complex (KRC) is a typical example.

The Katherina area (Fig. 1a) is characterized by emplacement of large bodies of weakly to un-deformed calc-alkaline plutonic and volcanic igneous associations from ca. 635 to 590 Ma (Moreno et al. 2012; Be'eri-Shlevin et al. 2009; Be'eri-Shlevin et al. 2011). Field investigations revealed that the KRC cross-cuts late Pan-African, subduction-related calc-alkaline granitoids and their volcanic equivalents (Bentor 1985; Garfunkel 1999). In the study area, the transition from calc-alkaline to alkaline magmatism is marked by the intrusion of spectacular dyke swarms of varying composition ranging from rhyolite to andesite and basalt. These dyke swarms cut across the calc-alkaline rocks but in turn are truncated by the KRC. The country rocks of the KRC in the investigated area are the Rutig volcanics and associated quartz-diorite. The quartz-diorite represents the oldest rock unit in the study area and yielded a single-crystal U-Pb zircon of 844 ± 4 Ma (Bea et al. 2009). The age of calc-alkaline granitoids is 610 ± 5 Ma (Be'eri-Shlevin et al. 2009), while the Rutig volcanics gave ages from 619 ± 4 to 607 ± 3 Ma (Be'eri-Shlevin et al. 2011).

The rock units of KRC in the study area include volcanics, subvolcanic rocks, ring dykes, and a granitic pluton. Based on field observations, the KRC started with explosive eruption of the Katherina volcanics and their pyroclastics, followed by emplacement of subvolcanics, ring dykes, and eventually the Katherina pluton. The available ages for the different rock units of the KRC (583–602 Ma; Be'eri-Shlevin et al. 2009; Moreno et al. 2012) clearly show that it postdates the Rutig volcanics.

The volcanic rocks include rhyolite, ignimbrite, and associated pyroclastics. The subvolcanic rocks include perthite granite and albite granite. The ring dykes are semicircular in shape and consist mainly of quartz syenite, quartz monzonite, and microgranite (Fig. 1a). The granitic pluton forming the inner core of the KRC is made up of alkaline syenogranite and alkali feldspar granite.

The syenitic rocks of Abu Rumeil form the inner ring dyke of the KRC (Fig. 1b). The dyke has a semicircular shape and highly variable width (few meters—1300 m). The dyke intrudes the Rutig and Katherina volcanics along sharp and subvertical contacts. In the northwestern part, it is cut by the Katherina pluton. It consists mainly of syenites with less quartz-monzonite and microgranite. The syenites include alkali feldspar syenite and quartz syenite. They have a red color and medium-grained texture. The alkali feldspar syenite is dominant and represents the early phase, while quartz syenite was emplaced later.

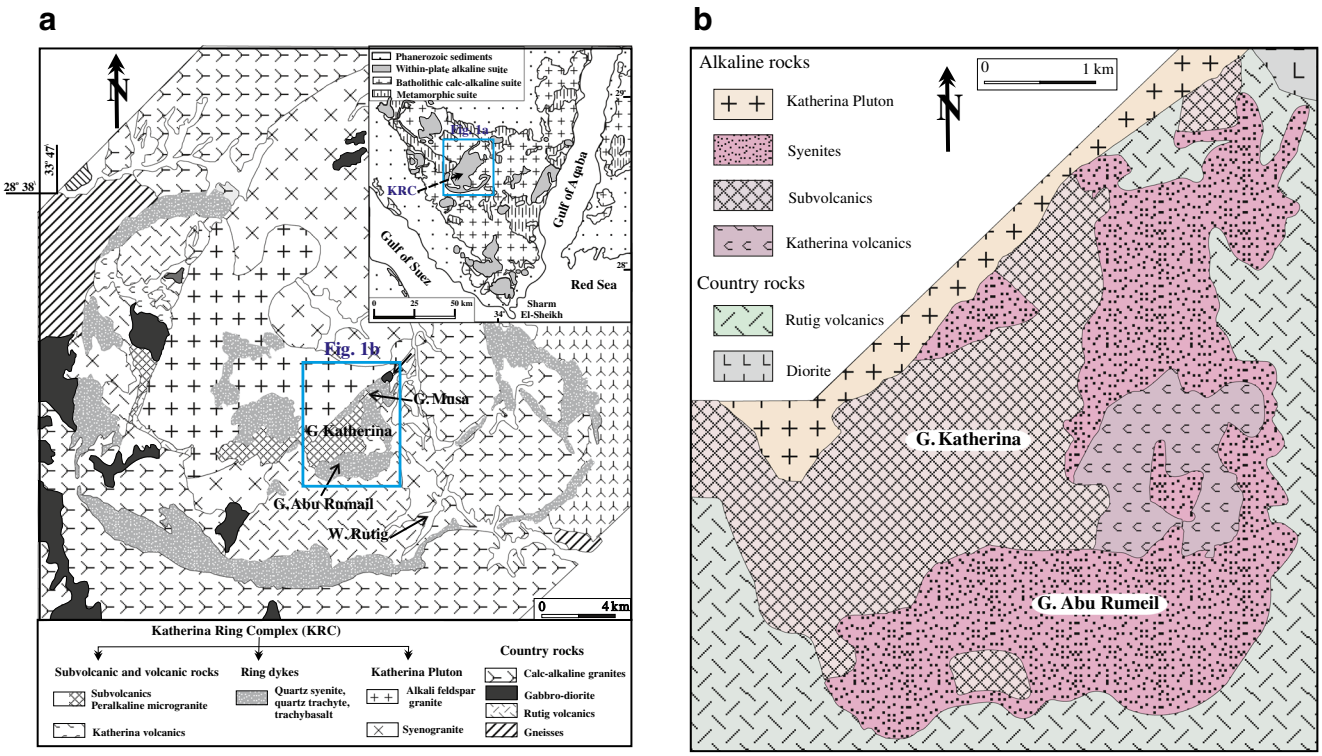

Fig. 1 **a** Geological map of the Katherina ring complex (modified after Katzir et al. 2007). *Inset* shows simplified geological map of the late Proterozoic rocks in south Sinai, and the location of the KRC is indicated. Also, the location of Fig. 1b is shown. **b** Geologic map of Abu Rumeil area (modified after Eyal et al. 2014)

Petrography

Based on petrographic studies, the syenitic rocks of Abu Rumeil are distinguished into alkali feldspar syenite and quartz syenite, the former being more abundant. The alkali feldspar syenite forms strips of dark brown to light red rocks in outcrop; it is fine- to medium-grained and exhibits hypidiomorphic and seriate textures. It is composed of alkali feldspar, plagioclase, amphiboles, pyroxenes, and subordinate biotite; quartz is entirely absent. Fe-Ti oxides, allanite, and apatite are the common accessory minerals. Feldspars are the dominant minerals and constitute about 65 % of the mode. Alkali feldspars are dusty in appearance and include both orthoclase and microcline. Perthitic texture is very common in the orthoclase. Microcline often exhibits microperthitic texture and Carlsbad twinning, sometimes overprinted by cross-hatch twinning (Fig 3a). Plagioclase occurs as isolated, corroded crystals showing simple twinning, usually associated with orthoclase. Pyroxene includes both clinopyroxene and orthopyroxene. Clinopyroxene is represented by augite and occurs as pale green, euhedral to subhedral crystals. Some augite crystals are twinned, zoned, and partially transformed into winchite (Fig. 2b) or other amphiboles (Fig. 2c). The orthopyroxene is enstatite rimmed by margins of secondary amphiboles. Primary amphiboles are represented by hornblende with rare of them overgrown by primary K-feldspars. Biotite is partly transformed into aggregates of muscovite (Fig 2d).

The quartz syenite of Abu Rumeil is a dark reddish brown porphyritic rock. Phenocrysts make up 50 to 75 % by volume. The groundmass is fine-grained but shows the same mineralogy as the phenocryst assemblage. Phenocrysts include K-feldspar (45–65 %), plagioclase (5–12 %), quartz (5–10 %), and mafic minerals (2–10 %). All of these show extensive corrosion and reaction rims (Fig. 2e–h). Accessory minerals are zircon, allanite, apatite, and monazite. The groundmass consists mainly of alkali feldspar and quartz, with lesser amounts of plagioclase, biotite, amphibole, and Fe-Ti oxides. The K-feldspar phenocrysts are mainly perthite (Fig. 2e), turbid, and stained with pale, reddish-brown color. Plagioclase occurs as both large corroded phenocrysts (Fig. 2f) and small laths in the groundmass. Quartz occurs as small anhedral crystals or interstitially in the groundmass. Mafic minerals are mostly pyroxene, hornblende, and biotite. Pyroxene includes both clinopyroxene and orthopyroxene. The former occurs as prismatic and tabular phenocrysts, partially replaced or rimmed by hornblende. Orthopyroxene is represented by anhedral crystals of enstatite. Sparse rounded xenocrysts of clinopyroxene (Fig. 2g) and small clinopyroxene inclusions in the orthoclase phenocrysts (Fig. 2h) are relicts of the mafic stages of evolution of the parental magma.

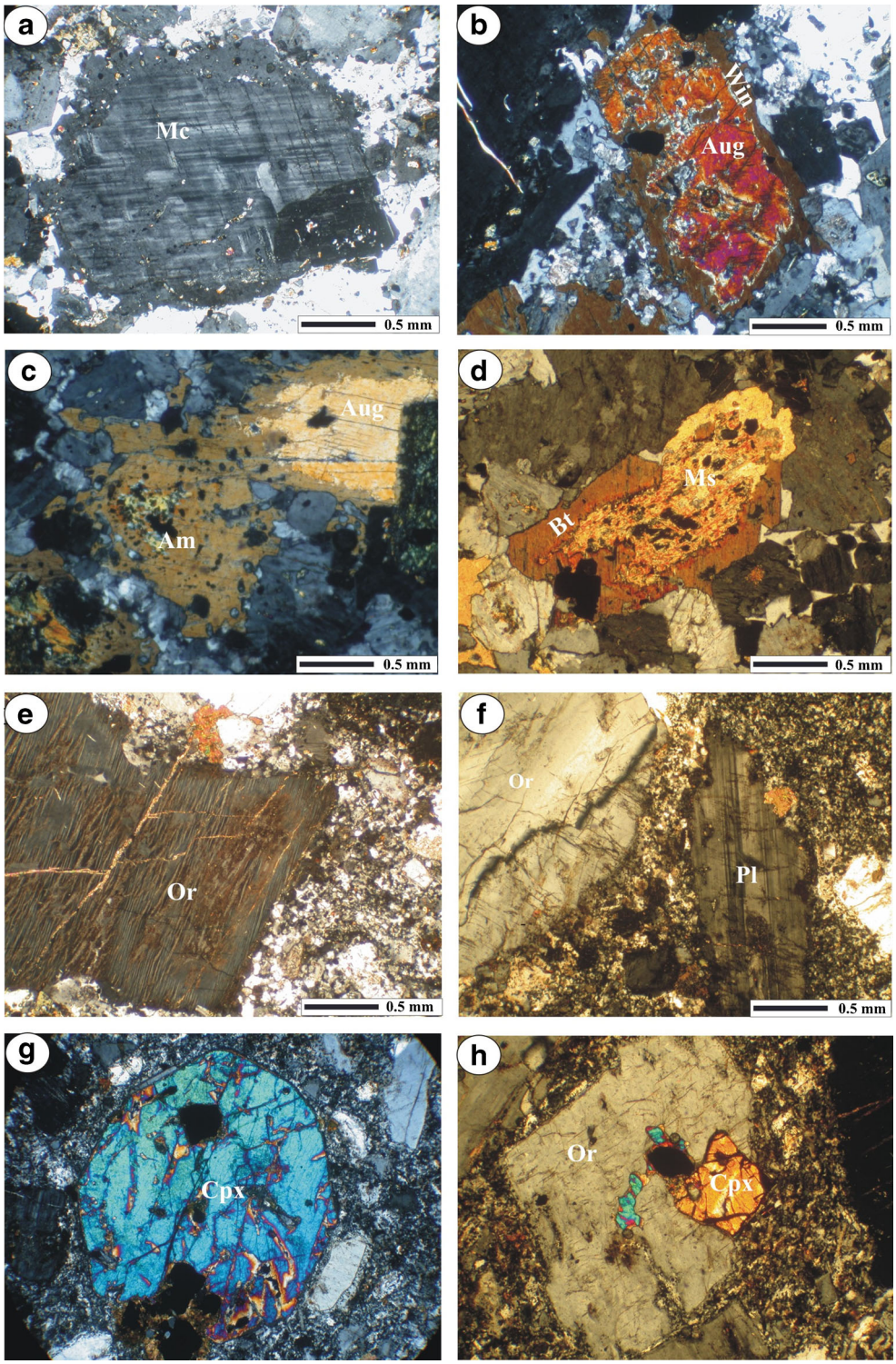

Fig. 2 Microphotographs of the syenitic rocks at Abu Rumeil area, all photomicrographs in cross-polarized light: **a** cross-hatched twinning in microcline, **b** augite crystal partly transformed into winchite, **c** augite crystal partly transformed into amphiboles, **d** biotite crystal partly transformed into aggregates of muscovite, **e** corroded orthoclase with perthite texture, **f** corroded plagioclase phenocryst associated with orthoclase, **g** rounded xenocryst of clinopyroxene, **h** small clinopyroxene inclusions in the orthoclase phenocrysts. The mineral abbreviations are *Mc* microcline, *Win* winchite, *Aug* augite, *Am* amphibole, *Bt* biotite, *Ms* muscovite, *Or* orthoclase, *Pl* plagioclase, and *Cpx* clinopyroxene

Analytical methods

Fifteen representative samples have been chemically analyzed for major and trace elements by X-ray fluorescence (XRF); 12 samples were carried out at the ACME Analytical Laboratories, Canada, and 3 samples were analyzed at the GeoAnalytical Lab, Washington State University, USA. The REEs for seven representative samples were determined by solution-source inductively coupled plasma mass spectrometry (ICP-MS) at the ACME Analytical Laboratories, Vancouver, Canada. The analytical precision for XRF analyses, as calculated from duplicate samples, is better than 1 % for most major elements and better than 5 % for most trace elements. Accuracy in this lab has been established by

analysis of established geostandards, whose accepted compositions are routinely recovered within the stated precision.

Mineral analyses and backscattered electron images were collected at the GPS Division Analytical Facility, California Institute of Technology, using a five-spectrometer JEOL JXA-8200 electron microprobe. The analytical conditions were 15 kV accelerating voltage, 25 nA beam current, a focused beam (1 μm), 20 s on-peak counting times, and a mix of natural and synthetic mineral standards. Also, some mafic minerals in the polished thin sections were analyzed using a Cameca SX50 and JEOL 8900 microprobes housed at the University of Nevada, Las Vegas, USA, with a similar protocol except for 20 nA beam current and defocused 5–10 μm beam size.

Mineral chemistry

Representative microprobe analyses of the major mineral phases from the investigated syenitic rocks are given in Tables 1, 2, 3, 4, and 5.

Representative feldspar analyses from alkali feldspar syenite and quartz syenite are listed in Table 1. They include plagioclase (oligoclase) and alkali feldspars (orthoclase and anorthoclase) (Fig. 3a); microcline would also be called orthoclase in this nomenclature. Orthoclase in the alkali feldspar syenite ranges in composition from $Or_{50.1}$ to $Or_{81.6}$, while those in the quartz syenite range from $Or_{45.2}$ to $Or_{86.2}$. The anorthoclase shows variation in composition ranging from $Or_{35.6}$ to $Or_{38.4}$. Plagioclase in the alkali feldspar syenite ranges from $An_{19.1}$ to $An_{29.8}$ with an average $An_{25.0}$. Plagioclase in the quartz syenites is slightly more sodic, ranging between An $_{9.6}$ and $An_{21.9}$ with an average $An_{16.5}$.

Pyroxene analyses from syenites are listed in Table 2. Two types of pyroxene are found; clinopyroxene is more abundant than orthopyroxene. No compositional zoning could be distinguished within individual pyroxene grains. According to the classification given by Morimoto et al. (1988), the clinopyroxene is classified as augite with minor pigeonite. The orthopyroxene is enstatite (Fig. 3b, c). Clinopyroxene has low Al_2O_3 (<2.01 wt.%), TiO_2 (<0.75 wt.%), and Na_2O (<0.67 wt.%), and its Mg# [(Mg/(Mg+Fe^{2+})] ranges from 0.54 to 0.73 with an average of 0.63. The enstatite contents of orthopyroxene range from 55.1 to 66.9 % (mole fraction), and its Mg# ranges between 0.56 and 0.64 with an average of 0.61.

Biotites are similar in both alkali feldspar and quartz syenites (Table 3): iron-rich, siliceous biotites (near annite) with FeO*/MgO ratio ranging from 1.35 to 2.52, with an average of 2.12. They show the chemical characteristics of primary igneous biotite as well as somewhat re-equilibrated magmatic instances (Fig. 3d). The composition of biotite can be used to discriminate the association of parental magma (Nachit et al. 1985; Abdel-Rahman 1994), and on the Al_2O_3 vs. $FeO_{(t)}$ biotite discrimination diagram of Abdel-Rahman (1994), the analyzed biotites plot in the field of alkaline suites (Fig. 3e).

Representative chemical analyses of the primary amphiboles are listed in Table 4. According to the classification of Leake (1997), they are calcic amphiboles classified as magnesio-hornblende (Fig. 3f).

Fe-Ti oxides include both magnetite and ilmenite (Table 5). Ti-rich magnetite (4.0–6.0 wt.% TiO_2) was observed in both rock types. Ilmenite is compositionally uniform with 46.1 to 47.3 wt.% FeO and 46.9 to 49.7 wt.% TiO_2. It is enriched in MnO (3.3–3.7 wt.%), perhaps due to substitution of Mn for Fe^{2+} with increasing oxygen fugacity under magmatic conditions (Deer et al. 1992).

Geochemical characteristics

Major and trace element analyses and calculated normative minerals of the Abu Rumeil syenites are given in Table 6. Normative mineral compositions of the syenites were calculated using the Minpet Software (Richard 1995). The norms indicate that the alkali feldspar syenite is, on average, higher in color index (7.91–10.37) than the quartz syenites (6.34–9.48), although there is significant overlap. The syenites have a wide range of silica contents (62.3–67.8 wt.% SiO_2), and thus, their differentiation indices (Thornton and Tuttle 1960) range from 78.8 to 90.6 (Table 6). They are all quartz-normative (1.4–3.2 vol.%); none of the analyzed samples contain the normative nepheline characteristic of undersaturated syenitic rocks. The syenites have relatively high abundances of total alkalis (9.96–11.35 wt.%), Al_2O_3 (15.33–17.31 wt.%), and Ba (982–2628 ppm). The chemical index of alteration (CIA = molecular [Al_2O_3 / (Al_2O_3 + CaO + Na_2O + K_2O)] × 100) in the studied syenites varies between 46.03 and 49.03 (Table 6), within the range of fresh rocks (45–55; Nesbitt and Young 1982).

In the classification of Streckeisen and Le Maitre (1979), the analyzed samples plot in the syenitic fields (Fig. 4a). All samples plot in the field of alkaline syenite in the total alkali-silica (TAS) diagram (Fig. 4b) and in the shoshonitic field in the K_2O vs. SiO_2 diagram (Fig. 4c). The studied samples are geochemically characterized by high total alkali metals (9.96–11.35 K_2O + Na_2O %), low TiO_2 (<0.99 wt.%), high $A1_2O_3$ (15.33–17.31 wt.%), and enrichment in the LILE. All these values are characteristic of shoshonitic rocks (Morrison 1980). Plotting the syenite data in the shoshonite field of the Th-Co diagram (Fig. 4d) further confirms their shoshonitic affinity. The agpaitic indices of the investigated syenites are more than 0.87 (Table 6), consistent with their alkaline affinity (Liégeois et al. 1998). They are

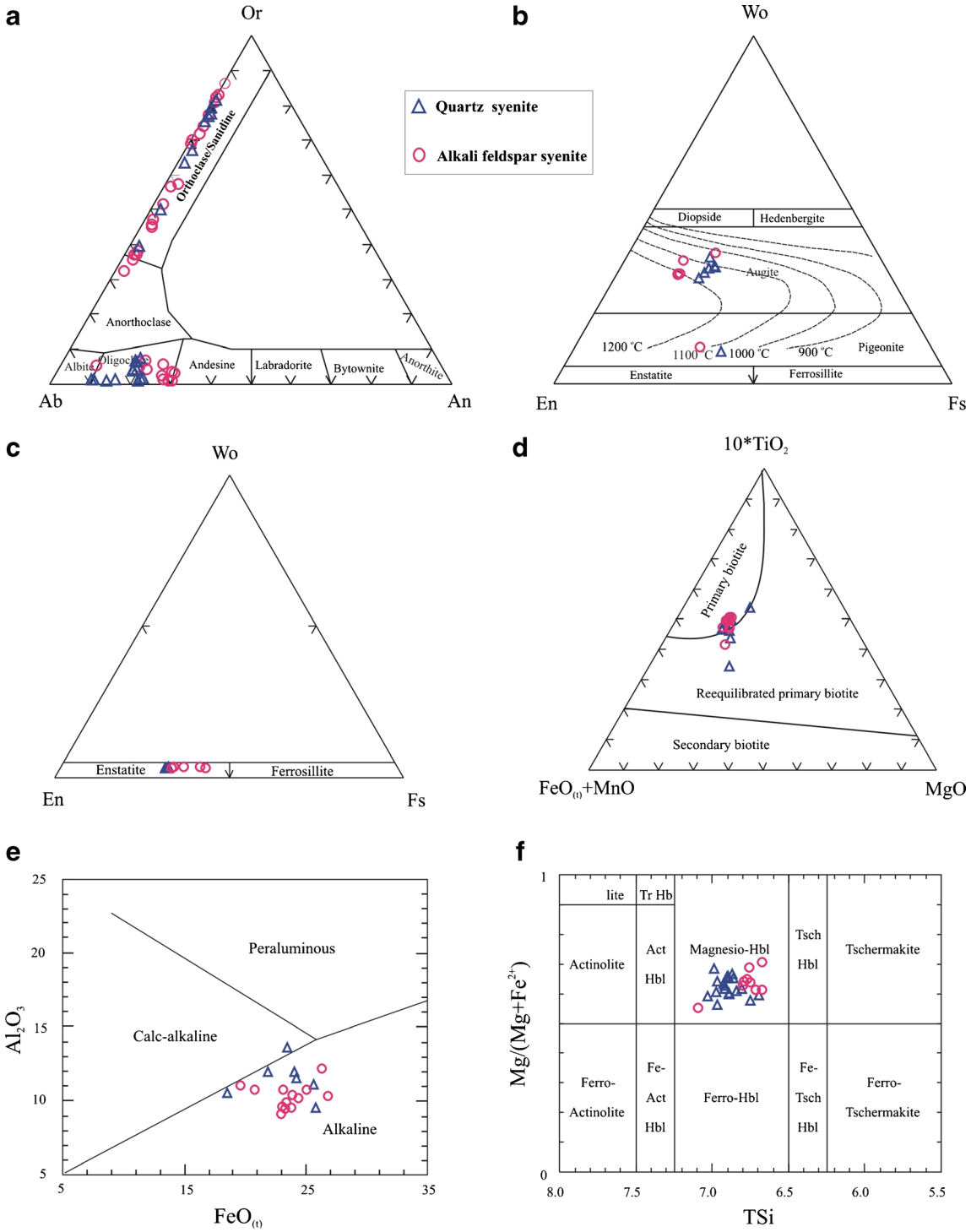

Fig. 3 **a** Or-Ab-An ternary diagram of the analyzed feldspars in the syenites (Deer et al. 1992). **b**, **c** Classification diagram of the pyroxene minerals (Morimoto et al. 1988); curves of temperature estimation are after Lindsley (1983). **d** TiO_2-$FeO_{(t)}$-MgO ternary diagram for the biotite of Abu Rumeil (Nachit et al. 2005). **e** $FeO_{(t)}$ vs. Al_2O_3 biotite discriminant diagram for the analyzed biotites (Abdel-Rahman 1994). **f** Classification of amphibole on the basis of Si and $Mg/(Mg + Fe^{2+})$ (Leake 1997)

metaluminous with ASI [=molar Al_2O_3 / ($CaO + K_2O + Na_2O$)] ranging between 0.86 and 0.97.

Selected major and trace elements for syenites are plotted against SiO_2 (Figs. 5 and 6). They show continuous trends with no compositional gap, although some elements show a break in slope at the boundary between alkali-feldspar syenites and quartz syenites at about 65 % SiO_2. Major elements show a clear decrease of

Table 1 Representative microprobe analyses (wt.%) of feldspars in the Abu Rumeil syenites

Rock type	Quartz syenite									Alkali feldspar syenite										
Sample no	103D									107D										
Mineral	K-feldspar					Plagioclase				K-feldspar					Plagioclase					
Analysis no.	326	328	333	346	367	765	766	768	772	742	743	745	762	764	359	360	377	379	748	
SiO_2	67.15	66.66	66.42	65.76	65.50	61.37	61.59	61.92	62.15	66.37	65.15	65.55	63.81	63.66	64.08	63.67	61.14	60.74	62.95	
TiO_2	0.04	0.03	0.07	0.06	0.01	0.11	0.09	0.07	0.10	0.10	0.07	0.03	0.07	0.02	0.11	0.08	0.10	0.11	0.09	
Al_2O_3	18.03	18.32	18.38	18.38	18.32	23.75	24.03	23.38	23.39	20.37	19.44	19.39	19.70	19.20	22.47	22.52	24.30	23.70	23.63	
FeO	0.32	0.21	0.18	0.31	0.15	0.28	0.30	0.30	0.28	0.59	0.51	0.30	0.24	0.18	0.27	0.29	0.25	0.33	0.31	
MgO	0.00	0.00	0.00	0.00	0.00	0.00	0.00	0.00	0.00	0.00	0.00	0.00	0.00	0.00	0.00	0.01	0.00	0.00	0.01	
CaO	0.13	0.07	0.10	0.35	0.08	4.71	4.65	3.95	3.95	0.49	0.36	0.08	0.17	0.20	4.13	4.23	5.89	5.27	4.52	
Na_2O	3.31	3.24	1.45	4.60	2.01	9.34	8.98	9.05	8.56	6.62	3.50	2.15	2.44	2.61	8.66	8.37	7.71	7.93	8.47	
K_2O	11.51	11.78	14.30	9.54	13.43	0.21	0.28	0.71	0.71	6.89	11.59	12.90	12.85	12.66	0.90	1.18	0.63	1.01	0.30	
Cr_2O_3	0.00	0.00	0.00	0.00	0.00	0.00	0.00	0.00	0.00	0.00	0.01	0.03	0.00	0.00	0.02	0.00	0.00	0.00	0.00	
MnO	0.01	0.00	0.00	0.02	0.02	0.00	0.00	0.01	0.00	0.01	0.00	0.00	0.00	0.01	0.00	0.00	0.03	0.00	0.01	
NiO	0.01	0.00	0.04	0.02	0.03	0.01	0.00	0.00	0.00	0.00	0.00	0.01	0.00	0.00	0.03	0.00	0.02	0.00	0.00	
Total	100.51	100.31	100.94	99.04	99.55	99.78	99.92	99.39	99.14	101.44	100.63	100.44	99.28	98.54	100.67	100.35	100.07	99.09	100.29	
Si	12.125	12.074	12.058	12.003	12.034	10.948	10.954	11.069	11.109	11.750	11.819	11.910	11.769	11.824	11.284	11.260	10.879	10.931	11.108	
Al	3.834	3.908	3.930	3.951	3.964	4.990	5.033	4.922	4.924	4.247	4.153	4.149	4.279	4.200	4.660	4.690	5.092	5.023	4.910	
Ti	0.005	0.004	0.010	0.008	0.001	0.015	0.012	0.009	0.013	0.013	0.010	0.004	0.010	0.003	0.015	0.011	0.013	0.015	0.012	
Fe_2	0.048	0.032	0.027	0.047	0.023	0.042	0.045	0.045	0.042	0.087	0.077	0.046	0.037	0.028	0.040	0.043	0.037	0.050	0.046	
Mn	0.002	0.000	0.000	0.003	0.003	0.000	0.000	0.002	0.000	0.001	0.000	0.000	0.000	0.002	0.000	0.000	0.005	0.000	0.001	
Mg	0.000	0.000	0.000	0.000	0.000	0.000	0.000	0.000	0.000	0.000	0.000	0.000	0.000	0.000	0.000	0.003	0.000	0.000	0.003	
Ca	0.025	0.014	0.019	0.068	0.016	0.900	0.886	0.757	0.756	0.093	0.070	0.016	0.034	0.040	0.779	0.802	1.123	1.016	0.855	
Na	1.159	1.138	0.510	1.628	0.716	3.231	3.097	3.137	2.967	2.273	1.231	0.757	0.873	0.940	2.957	2.870	2.660	2.767	2.898	
K	2.651	2.722	3.312	2.221	3.148	0.048	0.064	0.162	0.162	1.556	2.682	2.990	3.023	3.000	0.202	0.266	0.143	0.232	0.068	
Ab	30.20	29.40	13.30	41.60	18.50	77.30	76.50	77.30	76.40	58.00	30.90	20.10	22.20	23.60	75.10	72.90	67.80	68.90	75.80	
An	0.70	0.40	0.50	1.70	0.40	21.50	21.90	18.70	19.50	2.40	1.80	0.40	0.90	1.00	19.80	20.40	28.60	25.30	22.40	
Or	69.10	70.30	86.20	56.70	81.10	1.10	1.60	4.00	4.20	39.70	67.30	79.50	76.90	75.40	5.10	6.80	3.60	5.80	1.80	

Table 2 Representative microprobe analyses (wt.%) of pyroxenes in the Abu Rumeil syenites

Rock type	Quartz syenite											Alkali feldspar syenite										
Sample no.	103D											107D										
Mineral	Clinopyroxene							Orthopyroxene				Clinopyroxene						Orthopyroxene				
Analysis no.	No. 10	No. 12	No. 13	No. 15	No. 20	No. 3	No. 4	No. 11	No. 14	No. 15	No. 18	No. 1	No. 17	No. 18	No. 7	No. 8	759	No. 10	No. 2	No. 5	No. 6	No. 8
SiO_2	51.79	50.87	51.68	50.47	53.17	51.65	52.20	52.85	53.20	53.13	53.19	51.85	53.79	51.09	52.03	51.83	51.36	52.70	51.28	51.34	52.33	53.02
TiO_2	0.20	0.66	0.75	0.70	0.21	0.64	0.18	0.37	0.35	0.39	0.35	0.55	0.21	0.69	0.22	0.46	0.23	0.33	0.36	0.37	0.39	0.39
Al_2O_3	0.49	1.49	2.12	1.76	1.13	1.65	0.78	0.85	0.77	1.04	0.77	1.56	1.58	2.01	0.48	0.90	0.69	0.82	0.48	0.57	1.00	0.94
Cr_2O_3	0.24	0.01	0.02	0.01	0.00	0.01	0.02	0.09	0.00	0.01	0.02	0.03	0.00	0.00	0.17	0.24	0.00	0.00	0.16	0.09	0.00	0.01
FeO	14.88	15.02	13.83	15.61	22.61	14.95	13.70	18.31	18.50	18.72	18.81	10.84	19.31	10.01	10.88	10.95	14.15	19.20	24.86	24.03	20.68	19.39
MnO	0.76	1.31	1.26	1.24	2.37	0.65	1.13	1.15	1.17	1.15	1.16	0.87	1.65	0.72	0.77	0.63	1.55	1.31	1.50	1.51	1.73	1.43
MgO	13.10	11.31	13.63	11.45	14.92	12.06	11.38	24.39	24.20	23.83	23.67	15.53	16.59	14.43	16.26	16.05	10.83	23.30	19.63	20.24	21.87	23.10
CaO	17.82	18.32	16.67	18.34	4.78	18.05	19.71	1.56	1.61	1.67	1.69	17.71	5.55	19.58	17.80	17.86	20.76	1.67	1.64	1.68	1.67	1.68
Na_2O	0.53	0.35	0.53	0.48	0.34	0.47	0.34	0.04	0.04	0.06	0.06	0.44	0.43	0.67	0.41	0.34	0.45	0.04	0.06	0.05	0.06	0.05
K_2O	0.00	0.05	0.02	0.03	0.00	0.05	0.01	0.02	0.01	0.02	0.05	0.04	0.10	0.03	0.02	0.01	0.03	0.01	0.01	0.03	0.02	0.02
NiO	0.00	0.00	0.00	0.00	0.00	0.00	0.00	0.00	0.00	0.00	0.00	0.00	0.00	0.00	0.00	0.00	0.00	0.00	0.00	0.00	0.00	0.00
Total	99.81	99.39	100.51	100.09	99.53	100.18	99.45	99.63	99.85	100.02	99.77	99.42	99.21	99.23	99.04	99.27	100.05	99.38	99.98	99.91	99.75	100.03
TSi	1.965	1.956	1.939	1.925	2.053	1.960	1.999	1.946	1.957	1.954	1.963	1.939	2.049	1.914	1.949	1.940	1.960	1.957	1.945	1.940	1.955	1.960
TAl	0.022	0.044	0.061	0.075	0.000	0.040	0.001	0.037	0.033	0.045	0.033	0.061	0.000	0.086	0.021	0.040	0.031	0.036	0.021	0.025	0.044	0.040
TFe_3	0.000	0.000	0.000	0.000	0.000	0.000	0.000	0.000	0.000	0.000	0.000	0.000	0.000	0.000	0.000	0.000	0.000	0.000	0.000	0.000	0.000	0.000
M_1Al	0.000	0.023	0.032	0.004	0.051	0.033	0.034	0.000	0.000	0.000	0.000	0.008	0.071	0.002	0.000	0.000	0.000	0.000	0.000	0.000	0.000	0.001
M_1Ti	0.006	0.019	0.021	0.020	0.006	0.018	0.005	0.010	0.010	0.011	0.010	0.015	0.006	0.019	0.006	0.013	0.007	0.009	0.010	0.011	0.011	0.011
M_1Fe_3	0.000	0.000	0.000	0.000	0.000	0.000	0.000	0.000	0.000	0.000	0.000	0.000	0.000	0.000	0.000	0.000	0.000	0.000	0.000	0.000	0.000	0.000
M_1Fe_2	0.246	0.309	0.184	0.324	0.084	0.266	0.310	0.000	0.000	0.000	0.000	0.110	0.000	0.172	0.081	0.084	0.377	0.000	0.000	0.000	0.000	0.000
M_1Cr	0.007	0.000	0.001	0.000	0.000	0.000	0.001	0.003	0.000	0.000	0.001	0.001	0.000	0.000	0.005	0.007	0.000	0.000	0.005	0.003	0.000	0.000
M_1Mg	0.741	0.648	0.762	0.651	0.859	0.682	0.650	0.987	0.990	0.989	0.990	0.866	0.923	0.806	0.908	0.896	0.616	0.991	0.985	0.987	0.989	0.988
M_1Ni	0.000	0.000	0.000	0.000	0.000	0.000	0.000	0.000	0.000	0.000	0.000	0.000	0.000	0.000	0.000	0.000	0.000	0.000	0.000	0.000	0.000	0.000
M_2Mg	0.000	0.000	0.000	0.000	0.000	0.000	0.000	0.352	0.337	0.318	0.313	0.000	0.019	0.000	0.000	0.000	0.000	0.299	0.125	0.153	0.229	0.285
M_2Fe_2	0.226	0.174	0.250	0.173	0.646	0.208	0.129	0.564	0.569	0.576	0.581	0.229	0.615	0.141	0.260	0.259	0.075	0.596	0.789	0.759	0.646	0.599
M_2Mn	0.024	0.043	0.040	0.040	0.078	0.021	0.037	0.036	0.036	0.036	0.036	0.028	0.053	0.023	0.024	0.020	0.050	0.041	0.048	0.048	0.055	0.045
M_2Ca	0.724	0.755	0.670	0.749	0.198	0.734	0.809	0.062	0.063	0.066	0.067	0.710	0.227	0.786	0.714	0.716	0.849	0.066	0.067	0.068	0.067	0.067
M_2Na	0.039	0.026	0.039	0.036	0.025	0.035	0.025	0.003	0.003	0.004	0.004	0.032	0.032	0.049	0.030	0.025	0.033	0.003	0.004	0.004	0.004	0.004
M_2K	0.000	0.002	0.001	0.001	0.000	0.002	0.000	0.001	0.000	0.001	0.002	0.002	0.005	0.001	0.001	0.000	0.001	0.000	0.000	0.001	0.001	0.001
WO	36.92	39.13	35.15	38.66	10.61	38.39	41.82	3.08	3.18	3.32	3.37	36.54	12.33	40.76	35.94	36.27	43.16	3.33	3.31	3.37	3.37	3.35
EN	37.77	33.61	39.99	33.59	46.07	35.69	33.60	66.94	66.48	65.86	65.58	44.58	51.29	41.79	45.68	45.36	31.33	64.69	55.13	56.56	61.34	64.17
FS	25.31	27.25	24.86	27.75	43.32	25.91	24.58	29.98	30.34	30.83	31.06	18.88	36.39	17.45	18.38	18.37	25.51	31.97	41.56	40.07	35.30	32.47

Table 3 Representative microprobe analyses (wt.%) of biotite in the Abu Rumeil syenites

Rock type	Quartz syenite							Alkali feldspar syenite												
Sample no.	103D							107D												
Analysis no.	No. 3	No. 4	No. 7	No. 9	373	374	375	No. 1	No. 11	No. 20	No. 22	No. 25	No. 27	No. 28	No. 31	No. 32	No. 33	No. 35	No. 36	No. 6
SiO_2	36.19	37.21	35.74	36.16	34.95	31.39	32.75	37.01	37.78	36.71	35.45	37.37	37.47	35.95	37.13	35.78	34.11	35.59	37.28	36.06
TiO^2	3.24	3.83	3.15	3.25	3.29	2.04	2.81	3.55	3.31	3.48	3.37	3.42	3.29	3.50	3.03	3.44	2.80	3.56	3.58	3.21
Al_2O_3	11.13	10.52	11.98	9.53	11.98	11.51	13.59	11.04	10.75	9.58	10.14	9.85	9.43	9.53	9.10	10.31	12.14	10.74	10.76	10.42
FeO	25.59	18.47	24.01	25.79	21.81	24.23	23.45	19.59	20.79	23.05	24.35	23.32	23.29	23.81	22.91	26.79	26.27	25.06	23.12	23.89
MgO	10.15	13.67	11.50	10.23	10.38	13.52	12.06	11.54	12.31	10.16	11.52	10.26	9.70	10.38	10.73	10.66	12.17	11.01	10.99	10.81
CaO	0.05	0.19	0.11	0.09	0.18	0.08	0.35	0.01	0.06	0.23	0.07	0.15	0.20	0.06	0.00	0.07	0.15	0.05	0.08	0.01
Na_2O	0.13	0.12	0.12	0.27	0.15	0.04	0.12	0.23	0.08	0.09	0.03	0.05	0.05	0.08	0.03	0.05	0.05	0.08	0.04	0.07
K_2O	8.63	9.49	9.31	8.78	7.44	4.60	5.06	9.21	9.44	8.77	8.23	8.61	8.69	8.71	9.03	8.31	5.49	9.02	7.76	9.04
Cr_2O_3	0.00	0.00	0.00		0.00	0.00	0.01	0.00	0.00	0.02	0.03	0.04	0.01	0.04	0.07	0.02	0.02	0.31	0.02	0.00
MnO	0.36	0.29	0.42	0.55	0.44	0.51	0.44	0.00	0.00	0.36	0.41	0.43	0.24	0.38	0.29	0.28	0.45	0.46	0.34	0.00
NiO	0.00	0.00	0.00	0.00	0.17	0.01	0.26	0.00	0.00	0.00	0.00	0.00	0.00	0.00	0.00	0.00	0.00	0.00	0.00	0.00
Total	95.47	93.79	96.34	94.65	90.79	87.93	90.90	92.18	94.52	92.45	93.60	93.50	92.37	92.44	92.32	95.71	93.65	95.88	93.97	93.51
Si	5.969	6.060	5.824	6.057	5.939	5.549	5.552	6.143	6.143	6.196	5.944	6.219	6.313	6.104	6.271	5.923	5.680	5.866	6.121	6.040
AlIV	2.031	1.940	2.176	1.880	2.061	2.396	2.448	1.857	1.857	1.804	2.002	1.781	1.687	1.896	1.729	2.010	2.320	2.085	1.879	1.960
AlVI	0.131	0.078	0.123	0.000	0.337	0.000	0.265	0.301	0.202	0.100	0.000	0.149	0.184	0.009	0.081	0.000	0.061	0.000	0.202	0.095
Ti	0.402	0.469	0.386	0.410	0.421	0.271	0.358	0.443	0.405	0.442	0.425	0.428	0.417	0.447	0.385	0.428	0.351	0.441	0.442	0.404
Fe_2	3.530	2.516	3.272	3.613	3.100	3.582	3.325	2.719	2.827	3.253	3.414	3.245	3.281	3.381	3.236	3.709	3.658	3.455	3.175	3.347
Cr	0.000	0.000	0.000	0.000	0.000	0.000	0.001	0.000	0.000	0.003	0.004	0.005	0.001	0.005	0.009	0.003	0.003	0.040	0.003	0.000
Mn	0.050	0.040	0.058	0.078	0.063	0.076	0.063	0.000	0.000	0.051	0.058	0.061	0.034	0.055	0.041	0.039	0.063	0.064	0.047	0.000
Mg	2.496	3.319	2.793	2.555	2.630	3.563	3.048	2.855	2.984	2.556	2.880	2.545	2.436	2.627	2.702	2.631	3.021	2.705	2.690	2.699
Ca	0.009	0.033	0.019	0.016	0.033	0.015	0.064	0.002	0.010	0.042	0.013	0.027	0.036	0.011	0.000	0.012	0.027	0.009	0.014	0.002
Na	0.042	0.038	0.038	0.088	0.049	0.014	0.039	0.074	0.025	0.029	0.010	0.016	0.016	0.026	0.010	0.016	0.016	0.026	0.013	0.023
K	1.816	1.972	1.935	1.876	1.613	1.037	1.094	1.950	1.958	1.888	1.760	1.828	1.868	1.887	1.946	1.755	1.166	1.897	1.625	1.932
Fe_FeMg	0.590	0.430	0.540	0.590	0.540	0.500	0.520	0.490	0.490	0.560	0.540	0.560	0.570	0.560	0.540	0.590	0.550	0.560	0.540	0.550
Mg_FeMg	0.410	0.570	0.460	0.410	0.460	0.500	0.480	0.510	0.510	0.440	0.460	0.440	0.430	0.440	0.460	0.410	0.450	0.440	0.460	0.450

Table 4 Representative microprobe analyses (wt.%) of amphiboles in the Abu Rumeil syenites

Rock type	Quartz syenite							Alkali feldspar syenite						
Sample no.	103D							107D						
Analysis no.	318	319	320	321	339	340	341	734	735	736	737	738	756	757
SiO_2	46.67	46.46	45.96	46.89	46.21	47.99	47.59	44.08	44.30	45.43	48.45	44.14	45.02	45.23
TiO_2	1.34	1.34	1.27	1.29	1.33	1.16	1.43	1.43	1.41	1.22	1.29	1.40	1.44	1.40
Al_2O_3	6.05	6.25	5.85	6.04	6.13	6.00	5.79	6.34	6.53	6.60	7.10	6.04	6.26	6.23
FeO	18.60	19.47	18.28	18.40	17.57	17.06	18.55	20.39	19.83	19.25	18.49	18.11	19.36	18.73
MgO	11.20	10.61	11.10	11.65	11.54	12.43	11.55	10.38	10.38	10.71	9.95	11.93	10.81	11.22
CaO	10.17	10.19	10.65	10.15	10.27	10.33	10.13	10.30	10.35	10.22	10.25	10.35	10.32	10.53
Na_2O	1.98	2.01	1.66	1.91	1.74	1.84	1.94	1.95	1.82	1.85	1.47	1.91	1.81	1.81
K_2O	0.89	0.87	0.81	0.89	0.91	0.89	0.85	0.94	0.88	0.84	0.89	0.92	0.85	0.84
Cr_2O_3	0.02	0.00	0.00	0.00	0.00	0.00	0.00	0.00	0.00	0.01	0.00	0.00	0.00	0.00
MnO	0.76	0.84	0.83	0.72	0.76	0.68	0.72	0.84	0.82	0.84	0.82	0.85	1.06	0.97
NiO	0.00	0.00	0.02	0.00	0.00	0.00	0.00	0.00	0.00	0.01	0.03	0.00	0.02	0.00
Total	97.68	98.04	96.43	97.94	96.46	98.38	98.55	96.65	96.32	96.98	98.74	95.65	96.95	96.96
TSi	6.917	6.892	6.920	6.900	6.907	6.986	6.965	6.674	6.712	6.796	7.095	6.676	6.752	6.772
Tal	1.056	1.092	1.037	1.047	1.079	1.014	0.998	1.130	1.165	1.163	0.905	1.076	1.106	1.098
TFe_3	0.027	0.017	0.043	0.053	0.014	0.000	0.037	0.195	0.123	0.041	0.000	0.249	0.142	0.130
TTi	0.000	0.000	0.000	0.000	0.000	0.000	0.000	0.000	0.000	0.000	0.000	0.000	0.000	0.000
Sum_T	8.000	8.000	8.000	8.000	8.000	8.000	8.000	8.000	8.000	8.000	8.000	8.000	8.000	8.000
Cal	0.000	0.000	0.000	0.000	0.000	0.015	0.000	0.000	0.000	0.000	0.320	0.000	0.000	0.000
CCr	0.002	0.000	0.000	0.000	0.000	0.000	0.000	0.000	0.000	0.001	0.000	0.000	0.000	0.000
CFe_3	0.815	0.828	0.716	0.901	0.826	0.838	0.834	0.904	0.902	0.956	0.501	0.914	0.917	0.849
CTi	0.149	0.150	0.144	0.143	0.150	0.127	0.157	0.163	0.161	0.137	0.142	0.159	0.162	0.158
CMg	2.475	2.346	2.491	2.556	2.572	2.698	2.520	2.343	2.344	2.388	2.172	2.690	2.417	2.504
CFe_2	1.463	1.571	1.543	1.310	1.356	1.239	1.399	1.482	1.488	1.411	1.763	1.128	1.369	1.366
CMn	0.095	0.106	0.106	0.090	0.096	0.084	0.089	0.108	0.105	0.106	0.102	0.109	0.135	0.123
CCa	0.000	0.000	0.000	0.000	0.000	0.000	0.000	0.000	0.000	0.000	0.000	0.000	0.000	0.000
Sum_C	5.000	5.000	5.000	5.000	5.000	5.000	5.000	5.000	5.000	5.000	5.000	5.000	5.000	5.000
BMg	0.000	0.000	0.000	0.000	0.000	0.000	0.000	0.000	0.000	0.000	0.000	0.000	0.000	0.000
BFe_2	0.000	0.000	0.000	0.000	0.000	0.000	0.000	0.000	0.000	0.000	0.000	0.000	0.000	0.000
BMn	0.000	0.000	0.000	0.000	0.000	0.000	0.000	0.000	0.000	0.000	0.000	0.000	0.000	0.000
BCa	1.615	1.619	1.718	1.600	1.645	1.611	1.588	1.671	1.680	1.638	1.608	1.677	1.658	1.689
BNa	0.385	0.381	0.282	0.400	0.355	0.389	0.412	0.329	0.320	0.362	0.392	0.323	0.342	0.311
Sum_B	2.000	2.000	2.000	2.000	2.000	2.000	2.000	2.000	2.000	2.000	2.000	2.000	2.000	2.000
ACa	0.000	0.000	0.000	0.000	0.000	0.000	0.000	0.000	0.000	0.000	0.000	0.000	0.000	0.000
Ana	0.184	0.198	0.203	0.145	0.149	0.131	0.139	0.243	0.215	0.175	0.026	0.237	0.185	0.215
AK	0.168	0.165	0.156	0.167	0.174	0.165	0.159	0.182	0.170	0.160	0.166	0.178	0.163	0.160
Sum_A	0.352	0.362	0.358	0.312	0.323	0.296	0.298	0.425	0.385	0.335	0.192	0.415	0.347	0.375

Al_2O_3, TiO_2, Fe_2O_3, MgO, CaO, and P_2O_5, while Na_2O and K_2O are constant with increasing SiO_2. Regarding trace elements, Rb, Nb, Y, Zr, Th, Ga, and Ta increase whereas Sr, Ba, and V decrease with increasing SiO_2 content. According to the criteria of Frost et al. (2001), the syenites of Abu Rumeil are ferroan A-type rocks (Fig. 7a). Furthermore, they plot in the field of A-type granites on a plot of Ga/Al vs. $FeO_{(t)}/MgO$ (Fig. 7b).

The REE concentrations of Abu Rumeil syenites are given in Table 7. Their chondrite-normalized REE patterns (using the chondrite values of Pearce 1983) are generally similar, but there are clear systematic trends (Fig. 7c). All samples show enrichment of light over heavy REE [$(La/Lu)_N$ = 7.58–25.17], with a surprising decrease in slope from the more primitive alkali feldspar syenites towards the more evolved quartz syenites. They display a wide range of Eu anomalies [(Eu/

Table 5 Representative microprobe analyses (wt.%) of Fe-Ti oxides in the Abu Rumeil syenites

Rock type	Quartz syenite												Alkali feldspar syenite	
Sample no.	103D												107D	
Mineral	Magnetite								Ilmenite				Magnetite	Ilmenite
Analyses no.	723	724	725	726	727	728	751	753	729	730	731	732	396	395
SiO_2	0.02	0.07	0.04	0.06	0.05	0.05	0.04	0.09	0.02	0.00	0.00	0.00	0.03	0.14
TiO_2	0.84	0.71	1.61	9.67	1.38	1.45	4.04	4.92	49.70	49.25	48.63	48.59	6.20	46.91
Al_2O_3	0.57	0.91	0.36	0.38	0.68	0.33	0.16	0.11	0.18	0.04	0.01	0.01	0.37	0.08
FeO	91.78	92.06	91.52	83.08	91.43	92.33	89.68	87.71	46.09	46.72	47.28	46.46	86.05	46.82
MgO	0.01	0.00	0.00	0.00	0.00	0.00	0.00	0.00	0.00	0.00	0.00	0.00	0.01	0.00
CaO	0.01	0.00	0.01	0.00	0.01	0.00	0.08	0.05	0.01	0.00	0.01	0.01	0.01	0.01
Na_2O	0.00	0.00	0.00	0.00	0.00	0.02	0.00	0.00	0.00	0.00	0.01	0.00	0.00	0.00
K_2O	0.00	0.00	0.01	0.01	0.00	0.00	0.01	0.14	0.00	0.00	0.00	0.00	0.01	0.01
Cr_2O_3	0.00	0.02	0.03	0.00	0.01	0.02	0.00	0.00	0.00	0.00	0.00	0.00	0.00	0.00
MnO	0.05	0.05	0.05	1.00	0.15	0.09	0.56	0.53	3.54	3.42	3.61	3.66	0.47	3.31
NiO	0.00	0.00	0.00	0.00	0.00	0.00	0.00	0.00	0.00	0.00	0.00	0.00	0.00	0.00
Total	93.28	93.82	93.62	94.21	93.71	94.28	94.57	93.55	99.53	99.44	99.55	98.74	93.15	97.28

$Eu^*)_n$ = 0.45–1.50], with increasingly negative Eu anomalies in the more evolved quartz syenites. Negative Eu anomalies (Eu/Eu = 0.45–1.13) in the quartz syenite suggest little feldspar accumulation in this rock, whereas the positive Eu anomaly (Eu/Eu = 1.48–1.50) in the alkali feldspar syenite could be consistent with a cumulate origin.

N-MORB-normalized multi-element diagrams for the averages of alkali feldspar syenite and quartz syenite (Fig. 7d) are again generally similar, but the more fractionated nature of the trace element pattern in the less-evolved alkali feldspar syenites is again evident. All patterns show about one order of magnitude enrichment in the LILE (K, Rb, and Ba) and Pb relative to HFSE (Nb, Ta, and Ti). This signature is generally consider to be due to enrichment by fluid addition and is often attributed to modification of magmatic sources by fluids derived from a subducting slab (Kay and Mahlburg-Kay 1991). The presence of such a signature in intra-plate magmas is puzzling, as discussed below.

Discussion and conclusions

The post-collisional phase (630–580 Ma) of the northernmost ANS included voluminous intrusion and eruption of calc-alkaline and alkaline magmatism (e.g., Be'eri-Shlevin et al. 2009; Eyal et al. 2010; Farahat and Azer 2011). The origin of this magmatism is controversial. A variety of petrogenetic models have been proposed for the post-collisional A-type magmatism of the ANS, including mantle origin with a significant crustal contribution (e.g., Stern and Voegeli 1987; Beyth et al. 1994; Kessel et al. 1998; Mushkin et al. 2003; Azer 2006; Samuel et al. 2007; Jarrar et al. 2008) and anatectic melts of various crustal sources (e.g., Clemens et al. 1986; Creaser et al. 1991; King et al. 1997; Abdel-Rahmen 2006; Ali et al. 2009). The data presented herein from the Abu Rumeil syenites address the nature and source of the parental magma as well as the conditions under which the suites of observed rocks were generated by magmatic differentiation processes.

Geotectonic affinities

Previous studies dealing with the tectonic setting of alkaline magmatism in southern Sinai have reached contradictory conclusions (e.g., Samuel et al. 2007; Azer 2013; Eyal et al. 2014). An important question is whether or not emplacement of alkaline rocks in southern Sinai was related to rifting. Some authors have concluded that the alkaline rocks of the KRC mark a non-orogenic period of tensional stress, block faulting, and differential uplift (Bentor 1985), while others considered them to be rift-related (Abdel Maksoud et al. 1993; Abdel Khalek et al. 1994). The syenitic rocks of southern Sinai are spatially associated with tectonic lineaments that developed either during or following the post-collisional phase. This spatial association, together with mantle-derived isotopic signatures (Moreno et al. 2014), suggests that parental magmas were derived from deep sources and that the lineaments formed conduits to reach the upper crust. Field investigations reveal that the syenites of Abu Rumeil represent the inner ring dyke of the KRC. The intrusion of the KRC was preceded by the intrusion of dykes with various compositions that cut across the late Neoproterozoic calc-alkaline rocks and mark the switch from calc-alkaline to alkaline magmatism, as a result of extension (Friz-Töpfer

Table 6 Chemical and normative compositions of the syenites of G. Abu Rumeil, south Sinai, Egypt

Rock type	Alkali feldspar syenite								Quartz-syenite						
Sample no.	101D	105B	105D	107D	111B	112D	121D	AZR	103B	103D	109B	113D	114B	115D	118B
Major oxides (wt.%)															
SiO_2	63.45	64.37	63.87	63.6	64.23	64.15	64.17	62.31	67.78	65.16	65.25	65.62	66.32	65.12	64.86
TiO_2	0.77	0.81	0.75	0.75	0.8	0.81	0.78	0.99	0.61	0.73	0.68	0.72	0.63	0.67	0.76
Al_2O_3	17.01	16.23	16.91	17.1	16.42	16.72	16.58	17.31	15.33	15.91	15.87	15.93	16.15	16.11	16.87
Fe_2O_3	3.42	3.48	3.36	3.36	3.57	3.41	3.24	4.17	3.01	3.17	3.28	3.02	3.04	3.13	3.14
MnO	0.1	0.11	0.13	0.12	0.14	0.14	0.13	0.14	0.13	0.12	0.14	0.13	0.14	0.15	0.12
MgO	0.73	0.75	0.81	0.71	0.78	0.76	0.62	1.07	0.36	0.78	0.65	0.66	0.54	0.53	0.61
CaO	2.12	1.89	2.33	2.28	2.02	2.05	1.72	3.01	0.99	1.94	1.86	1.12	1.31	1.33	1.53
Na_2O	5.94	5.43	5.54	5.25	5.76	5.84	5.78	5.24	5.57	5.54	5.74	5.37	5.26	5.63	5.67
K_2O	5.41	5.37	5.31	5.15	5.18	5.22	5.31	4.72	5.03	5.03	5.33	5.36	5.31	5.37	5.35
P_2O_5	0.32	0.24	0.34	0.25	0.24	0.32	0.26	0.41	0.12	0.24	0.21	0.23	0.21	0.25	0.24
LOI	0.42	0.67	0.53	0.22	0.37	0.62	0.52	0.41	0.61	0.48	0.5	0.89	0.47	0.55	0.33
Total	99.69	99.35	99.88	98.79	99.51	100	99.11	99.78	99.54	99.1	99.51	99.05	99.38	98.84	99.48
Trace elements (ppm)															
Rb	55	55	70	65	65	50	71	56	109	60	60	74	88	57	83
Sr	319	247	363	341	261	278	289	431	113	271	214	184	151	165	237
Ba	2139	1476	2265	2444	1587	1762	1707	2628	982	1807	1385	1362	1371	1258	1995
Nb	19	25	23	19.4	23	21	21	17.2	31.1	23	28	26	25	24	23
Th	9.5	12.2	10.3	7	11.6	9.9	10.2	7	15	13.4	13.7	14.1	13.6	12.8	12.6
U	2.3	3	3	3	2.8	3.1	2.4	2	5	3.7	3.4	4	4	3.5	3.2
Pb	19	26	12	14	20	23	14	12	21	24	21	31	17	22	24
Zr	315	405	312	304	383	351	361	268	541	360	452	424	415	417	332
Hf	7	9	8	–	9	8	8	–	–	9	10	10	11	10	9
Y	30	33	31	30	32	32	32	31	38	33	34	35	35	34	32
Ga	22.4	23.2	22.7	22	23.4	22.1	23.7	21	25	24.2	24.3	24.6	24.9	23.9	23.4
Ta	1.23	1.3	1.2	1.2	1.4	1.2	1.4	0.9	1.9	1.3	1.4	1.5	1.7	1.6	1.5
Cr	7	5	6	4	4	5	5	2	5	3	2	4	2	4	3
Sc	10.3	9.6	11.4	9	9.2	8.9	10.8	10	10	9.4	9.3	9.1	9.2	9.7	7.9
V	15	12	17	12	13	12	12	23	6	8	9	10	8	9	11
Cu	5	3	4	2	4	3	3	1	2	1	2	2	1	3	2
Zn	61	75	72	85	84	68	72	92	96	83	74	76	83	74	58
Ni	7	6	7	3	5	4	5	3	3	5	4	3	2	3	4
Co	6	3	5	–	4	4	3	–	–	3	2	1	1	2	4
Petrochemical parameters															
Na_2O/K_2O	1.10	1.01	1.04	1.02	1.11	1.12	1.09	1.11	1.11	1.10	1.08	1.00	0.99	1.05	1.06
AI	0.92	0.91	0.88	0.83	0.92	0.91	0.92	0.79	0.95	0.92	0.96	0.92	0.89	0.94	0.90
ASI	0.88	0.90	0.89	0.94	0.88	0.89	0.91	0.91	0.94	0.89	0.86	0.96	0.97	0.93	0.95
CIA	46.61	47.16	46.96	48.22	46.67	46.82	47.42	47.40	48.30	46.79	46.04	48.86	49.03	47.94	48.51
Normative composition (CIPW)															
Quartz	3.15	7.32	5.59	7.28	5.76	5.17	6.56	5.86	13.93	8.88	7.12	10.28	11.33	8.2	8.3
Orthoclase	32.29	32.25	31.67	30.96	30.97	31.11	34.31	28.16	33.15	30.22	31.9	32.35	31.8	32.37	33.34
Albite	50.77	46.69	47.31	45.19	49.3	49.84	46.29	44.77	43.51	47.65	49.19	46.4	45.11	48.59	45.17
Anorthite	3.79	4.1	5.62	8	3.67	4.01	4.28	9.85	2.76	3.73	1.8	3.59	4.82	2.87	5.98
Diopside	3.97	3.22	3.18	1.55	4.1	3.47	2.25	2.11	1.22	3.73	5.19	0.46	0.32	1.87	0.1
Hypersthene	2.83	3.29	3.43	4.02	3.08	3.11	3.23	5.2	3.33	2.9	2.07	4.09	4.05	3.32	4.17
Magnetite	0.94	0.98	0.93	0.94	1	0.96	0.92	1.17	0.81	0.89	0.91	0.86	0.84	0.88	0.89
Ilmenite	1.48	1.56	1.44	1.45	1.54	1.55	1.51	1.9	0.98	1.41	1.31	1.4	1.21	1.3	1.46
Apatite	0.71	0.53	0.75	0.56	0.53	0.7	0.58	0.9	0.27	0.53	0.46	0.51	0.46	0.56	0.53
Color index	9.22	9.05	8.98	7.96	9.71	9.09	7.91	10.37	6.34	8.93	9.48	6.81	6.43	7.36	6.62
Diff. index	86.22	86.26	84.57	83.43	86.02	86.13	87.17	78.79	90.59	86.75	88.2	89.03	88.24	89.16	86.81

1991). These dykes are in turn intruded by the alkaline phase, which represents the youngest igneous activity in the study area.

The geochemical affinity and mineral chemistry of the Abu Rumeil syenites are consistent with post-collisional activity and a within-plate tectonic setting. In the tectonic discrimination diagram of Pearce et al. (1984), they plot in post-collisional and within-plate fields (Fig. 8a). Geochemically, all the syenites are oversaturated despite their alkaline affinity; undersaturated rocks are not observed. This is inconsistent with the character of magmatism developed in intra-continental rifts (Black et al. 1985; Wilson 1994; Menuge et al. 2002). Classifications based on the mafic magmatic minerals in the Abu Rumeil syenites are consistent with this tectonic inference. In particular, the analyzed biotites are mostly

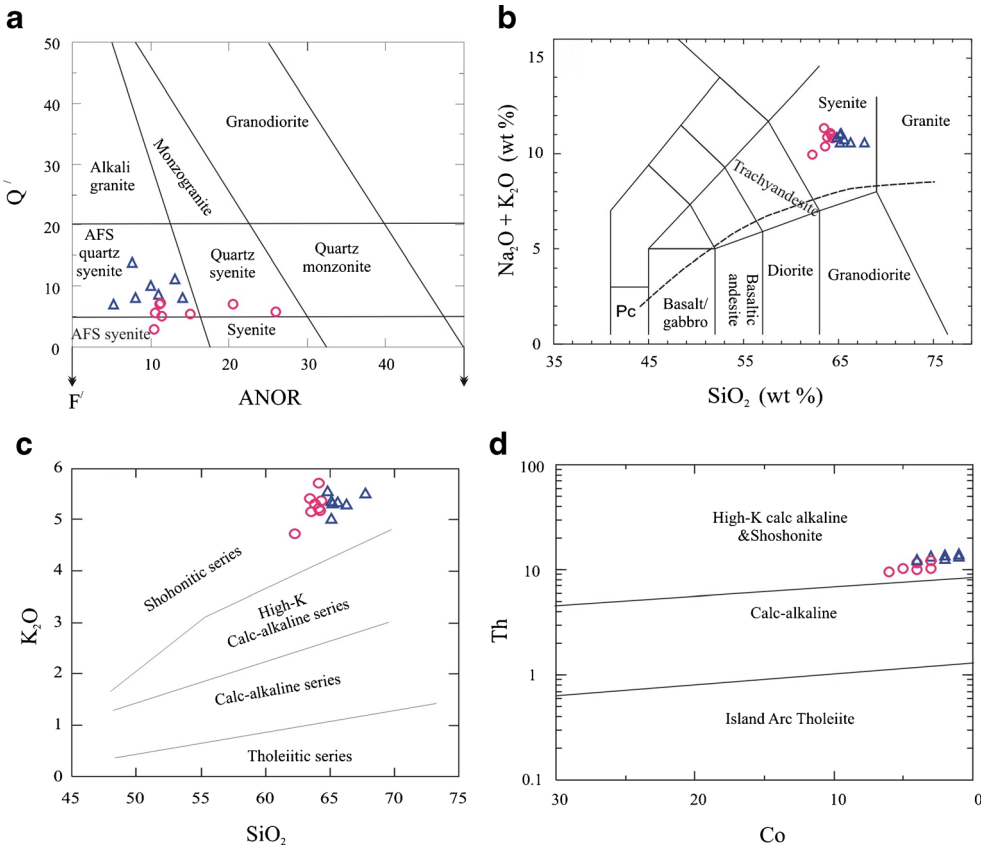

Fig. 4 **a** Q/(F/)-ANOR diagram for normative classification of Abu Rumeil syenites (Streckeisen and Le Maitre 1979). **b** Total alkalis vs. silica (TAS) diagram (Le Bas et al. 1986) with the discriminating boundary between alkaline and sub-alkaline fields after Miyashiro (1978). **c** SiO_2 vs. K_2O plots (Pearce et al. 1990). **d** Co vs. Th diagram; the field demarcations are after Hastie et al. (2007). *Symbols* are as in Fig. 3

iron-rich and similar to biotites of alkaline igneous rocks of anorogenic tectonic settings (Abdel-Rahman 1994).

Petrogenetic source

In general, alkaline syenitic rocks associated with A-type granites have been described from various A-type complexes worldwide (Bonin 2007; Whalen et al. 1987; Liégeois et al. 1998; Azer 2006; Jahn et al. 2009; Litvinovsky et al. 2011). Several petrogenetic models have been proposed for the formation of syenites, which mainly include (1) fractionation from mantle-derived basaltic-andesitic magmas (e.g., Currie 1989; Sutcliffe et al. 1990; Litvinovsky et al. 2002; Yang et al. 2005; Bonin 2007; Turner et al. 1992; Miyazaki et al. 2003; Conceição and Green 2004; Wang et al. 2005; Shellnutt et al. 2009), (2) partial melting of crustal material (Whalen et al. 1987; Allen and Chappell 1992; Lubala et al. 1994; Tchameni et al. 2001; Jahn et al. 2009; Litvinovsky et al. 2011), and (3) interaction between mantle-derived magmas and crustal rocks followed by subsequent differentiation of the resulting hybrid melts (e.g., Zhao et al. 1995; Stevenson et al. 1997; Litvinovsky et al. 1999; Mingram et al. 2000; Vernikovsky et al. 2003; Jung et al. 2007; Ying et al. 2007).

In southern Sinai, the syenitic rocks are rare and are closely associated with A-type granitoids. Previous discussions of the genesis of southern Sinai syenitic rock have focused on their close association with granites, rather than the individual petrological character of the syenites themselves. All petrogenetic models agree that A-syenites in southern Sinai were emplaced in post-collisional and within-plate tectonic settings. The studied syenites have a shoshonitic character, but the origin of shoshonitic syenites is also a matter of debate. Echoing the conflicting theories proposed for syenites worldwide, the A-type igneous rock suites in the ANS including southern Sinai have been attributed either to extensive fractional crystallization of mantle-derived magmas (e.g., Stern and Gottfried 1986; Bonin 2007) to partial melting of crustal material (e.g., Clemens et al. 1986; Creaser et al. 1991; King et al. 1997; Abdel-Rahmen 2006; Farahat et al. 2007; Ali et al. 2009) or to a mantle source with extensive crustal contamination (e.g., Azer 2007; Samuel et al. 2007; Be'eri-Shlevin et al. 2009).

In the following discussion, we will argue that the present data can rule out both end-member models of pure mantle source or pure crustal source. Both components are required, but the dominant petrogenetic mechanism is differentiation from mantle-derived mafic magmas, as often advocated for the ANS A-type igneous rocks (e.g.,

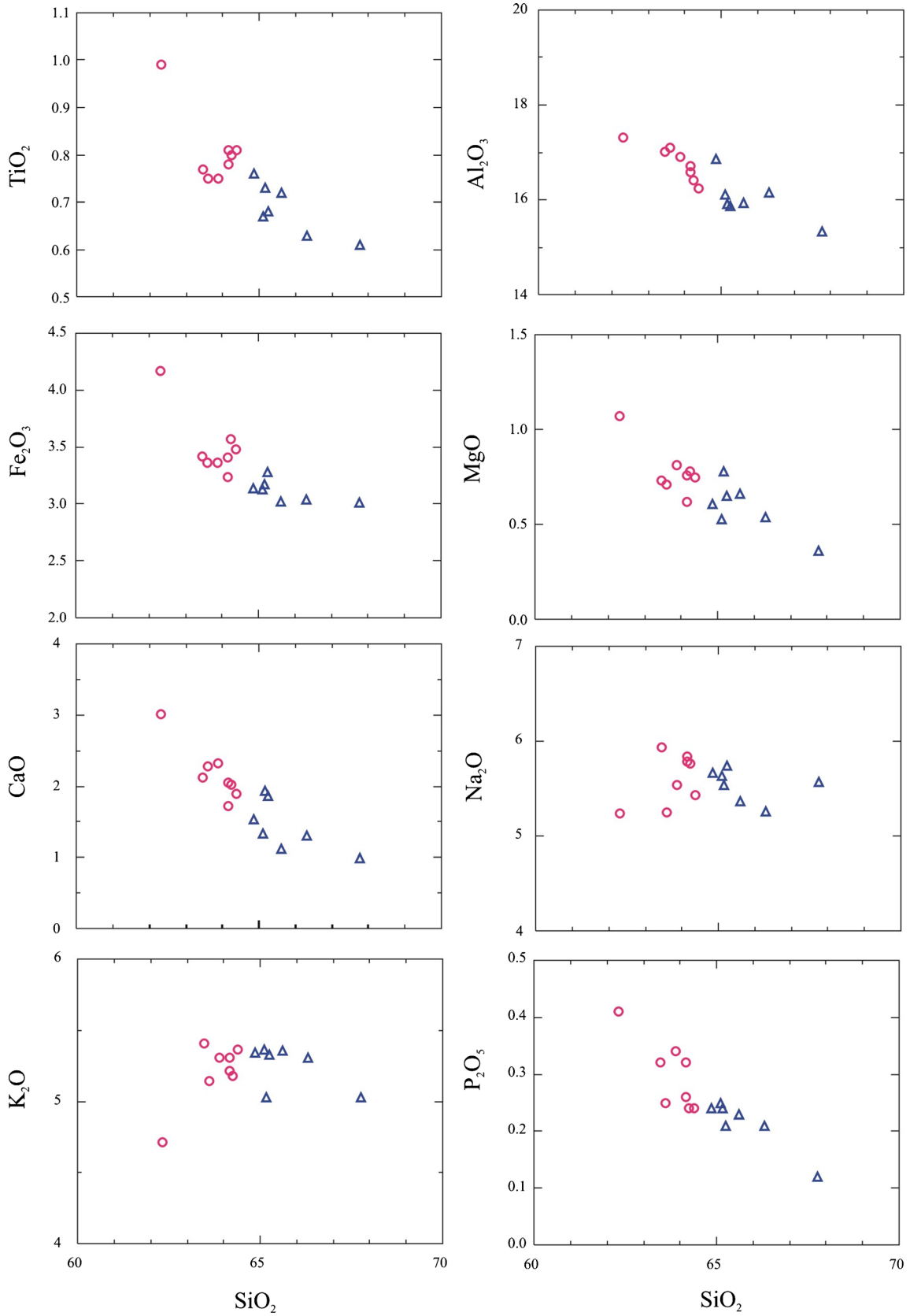

Fig. 5 Silica variation diagrams of major oxides for the syenites of Abu Rumeil. *Symbols* are as in Fig. 3

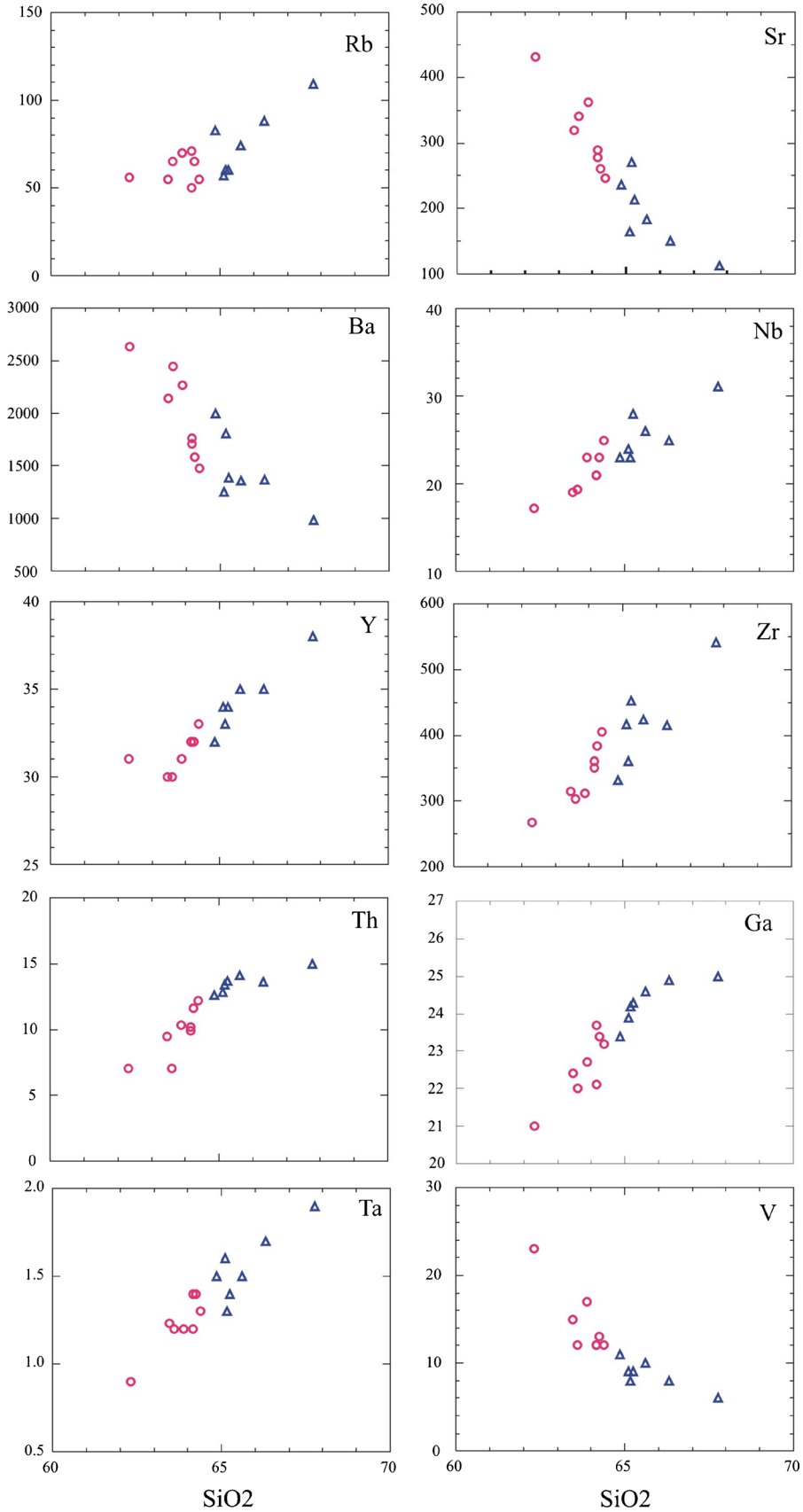

Fig. 6 Silica variation diagrams of some trace elements for the syenites of Abu Rumeil. *Symbols* are as in Fig. 3

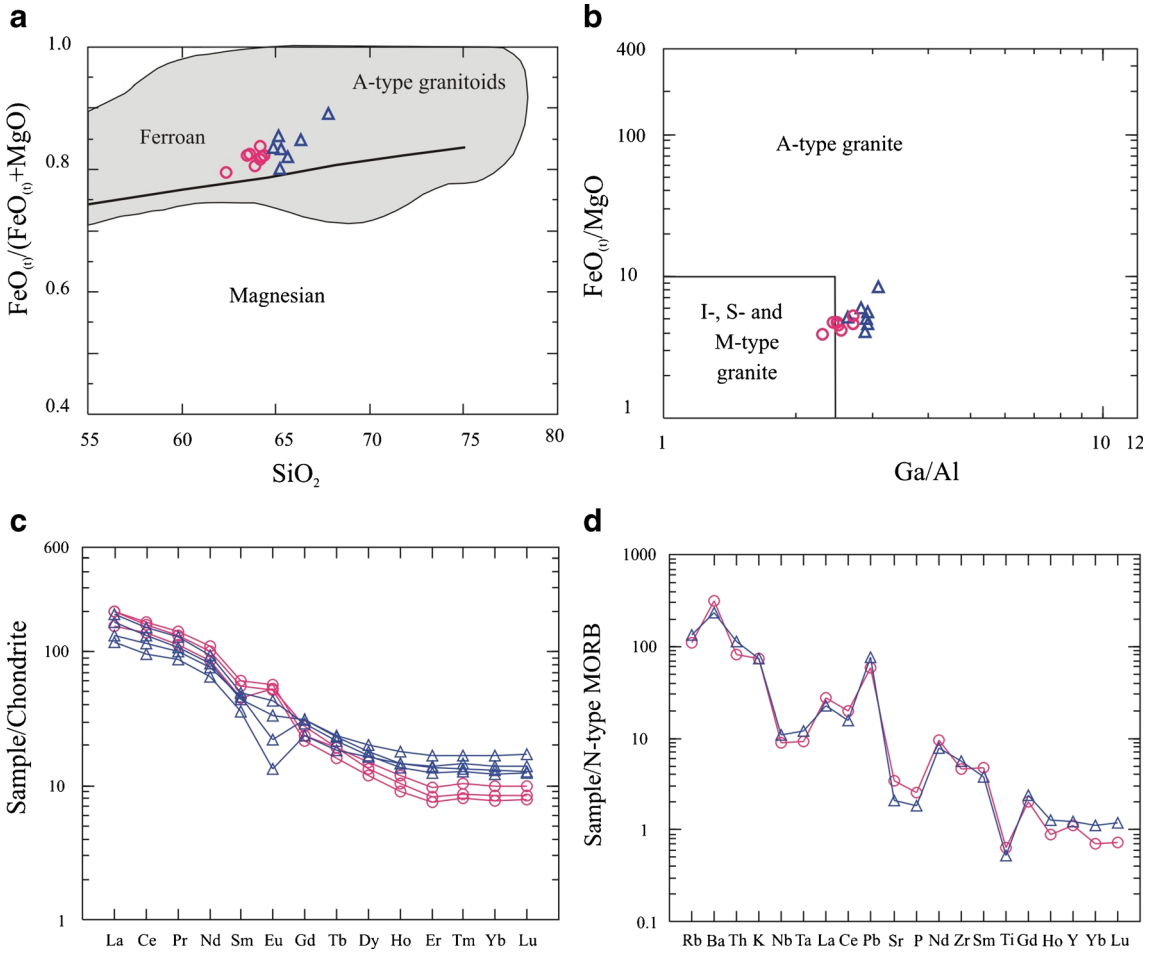

Fig. 7 **a** $FeO_{(t)}/(FeO_{(t)} + MgO)$ vs. SiO_2 diagram for the studied syenites (Frost et al. 2001). **b** Ga/Al vs. $FeO_{(t)}/MgO$ (Whalen et al. 1987). **c** Chondrite-normalized REE plots. **d** NMORB-normalized multi-element diagrams for the averages of alkali feldspar syenite and quartz syenite. *Symbols* are as in Fig. 3

Stern and Voegeli 1987; Beyth et al. 1994; Kessel et al. 1998; Mushkin et al. 2003; Jarrar et al. 2008), with relatively minor crustal contamination. We do have isotope data on the Abu Rumeil suite, but a number of other syenitic rocks in southern Sinai have isotope signatures (Hf, U, and Pb) indicating a predominantly mantle rather than crustal source (Morag et al. 2011).

Syenitic magmas can occur in the silica undersaturated or saturated alkaline igneous series (Lameyre and Bowden 1982). Silica-saturated syenites can be related to the sodic (Na_2O/K_2O >2; Le Maitre 2002) or shoshonitic series ($Na_2O/K_2O \approx 1$; Morrison 1980). The studied syenites are silica saturated and have Na_2O/K_2O ratios (0.99–1.11) characteristic of shoshonitic rocks. The shoshonitic series can be produced by decompression melting of a metasomatized mantle containing small amounts of phlogopite and pargasite (Conceição and Green 2004). The syenitic rocks of Abu Rumeil are characterized by high $K_2O + Na_2O$ (9.96–11.35 wt.%). Although high alkali concentrations are characteristic of evolved crustal rocks, numerous

Table 7 Rare earth element (ppm) concentrations and significant elemental ratios of the Abu Rumeil syenites

Rock type	Alkali feldspar syenite			Quartz syenite			
Sample no.	101D	105D	112D	114B	109B	113D	118B
La	73.80	56.40	73.70	43.50	61.10	48.10	69.20
Ce	158.40	132.50	153.30	92.60	127.20	110.30	145.50
Pr	19.44	15.33	18.19	11.93	14.76	13.75	17.61
Nd	78.10	60.40	71.20	46.30	57.40	54.50	66.50
Sm	13.98	10.40	12.84	8.18	10.16	10.57	11.38
Eu	4.87	4.61	4.51	1.15	2.92	1.93	3.72
Gd	7.25	8.54	6.61	7.31	9.55	9.59	8.82
Tb	1.11	1.13	0.94	1.08	1.33	1.38	1.24
Dy	5.12	5.72	4.59	6.23	6.86	7.64	6.33
Ho	0.88	1.01	0.77	1.24	1.26	1.52	1.17
Er	2.08	2.44	1.88	3.45	3.39	4.14	3.14
Tm	0.31	0.37	0.29	0.52	0.48	0.60	0.45
Yb	2.08	2.44	1.93	3.45	3.22	4.14	3.04
Lu	0.32	0.38	0.30	0.53	0.49	0.65	0.48
ΣREE	367.74	301.67	351.05	227.47	300.12	268.81	338.58
Eu/Eu	1.48	1.49	1.50	0.45	0.91	0.59	1.13
(La/Yb)n	23.99	15.63	25.82	8.53	12.83	7.86	15.39
(La/Sm)n	3.33	3.42	3.62	3.36	3.80	2.87	3.84
(Gd/Lu)n	2.78	2.75	2.70	1.69	2.39	1.81	2.25
(Ce/Yb)n	19.73	14.07	20.57	6.95	10.23	6.90	12.40
(La/Lu)n	23.63	15.21	25.17	8.41	12.78	7.58	14.77

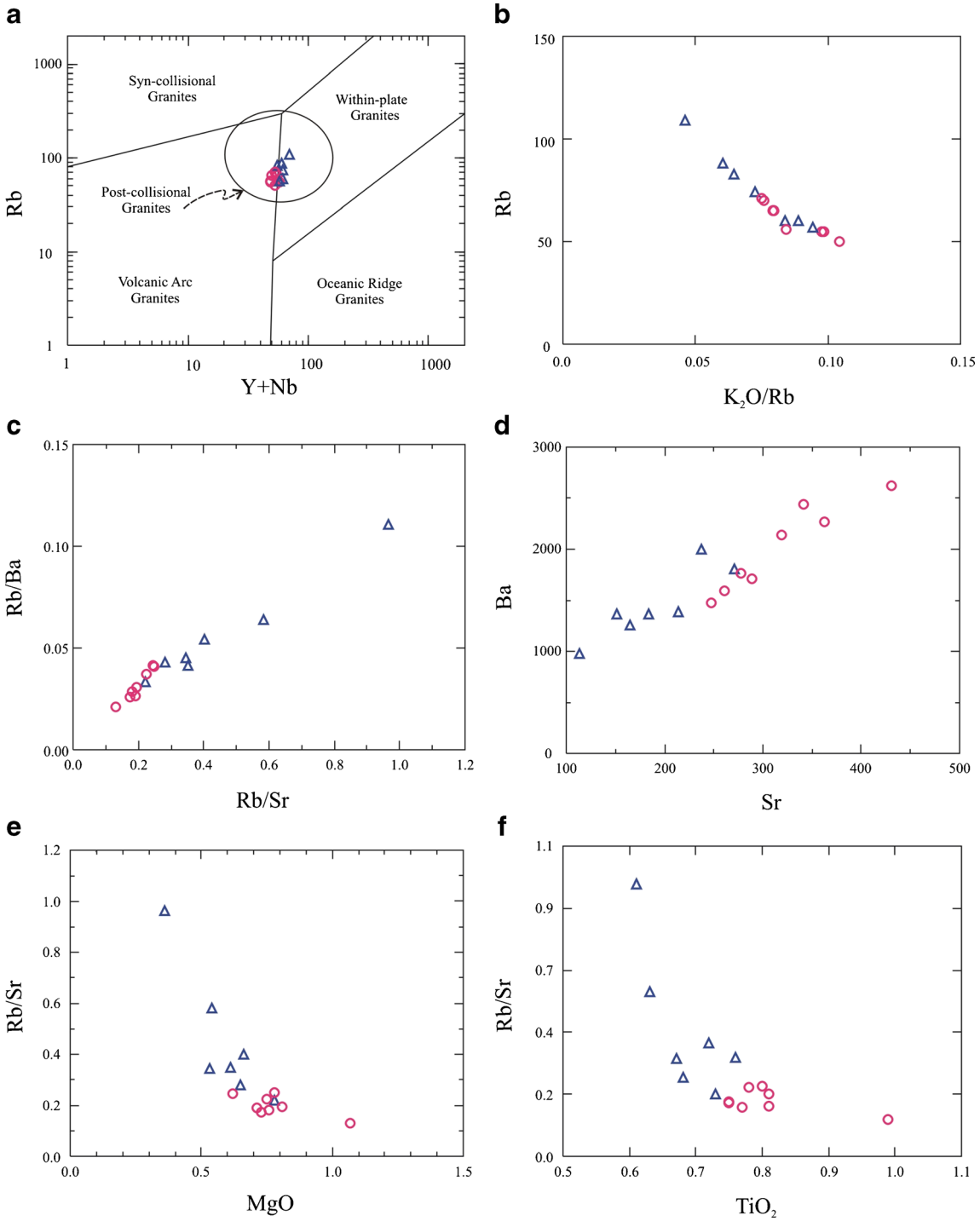

Fig. 8 **a** Rb vs. Y + Nb diagram for the syenites of Abu Rumeil (Pearce et al. 1984). **b**–**f** Some major and trace element relationships in the syenites of Abu Rumeil. *VAG* volcanic-arc granites, *syn-COLG* syn-collisional granites, *WPG* within-pate granites, *ORG* ocean-ridge granites. Post-collisional granite field is from Pearce (1996). *Symbols* are as in Fig. 3

geochemical and experimental studies (Conceição and Green 2004) argue that such high-alkali rocks are commonly derived from K-enriched basaltic and andesitic mantle magmas, with only a minor crustal contribution. The positive Eu anomaly and low Th/Ce ratios (0.06–0.15) in the more mafic members of the Abu Rumeil syenites indicate that crustal contamination, at least in the alkali-feldspar syenites, was limited (Taylor and McLennan 1995; Sun and McDonough 1989). Furthermore, experiments show that syenites and melts plausibly parental to syenites are not produced directly by anatexis of common crustal sources (Montel and Vielzeul 1997).

However, direct derivation of these syenites from a mantle source is difficult to reconcile with the available geochemical data, which indicate some role for crustal contribution during the evolution of syenites. Overlap in the REE patterns of the studied syenites excludes simple fractional crystallization as the sole process of magma evolution; differentiation must have been accompanied by some assimilation, most likely a crustal contribution. Finally, there is textural evidence for a contamination process. There are large mafic xenocrysts overgrown by primary K-feldspars. They show a spongy cellular texture due to the dissolution of crystals by the enclosed magma under disequilibrium conditions. These xenocrysts may represent either a remnant high-temperature phase that crystallized at greater depths or possibly entrapped crystals. In either case, they point to a petrogenesis involving mafic, presumably mantle-derived magma interacting with an evolved component.

The studied syenites have moderate depletion in Ta-Nb relative to the neighboring LILE, which is a geochemical characteristic feature of subduction-related magmas. Moreover, they show Ti depletion as commonly observed in subduction-related magmas. Shoshonitic rocks from continental within-plate settings may exhibit either arc-type geochemical features (Wyborn 1992; Leat et al. 1998) or OIB-type ones (Rogers et al. 1998). Since active subduction is not considered plausible in the within-plate post-collisional tectonic setting of the ANS, the subduction signature for the studied syenites is presumably inherited, due to partial melting of a lithospheric mantle source following a previous subduction event beneath the ANS (Azer et al. 2012; Khalil et al. 2015). This interpretation is not unique at this time; other means of inheriting a subduction signature could be proposed, and further data may be required to distinguish among them.

Crystallization conditions

The chemistry of some minerals can be used to elucidate and constrain both parental magma composition and the magmatic conditions at which they crystallized (e.g., Lindsley 1983; Blundy and Holland 1990; Putirka 2008; Ridolfi et al. 2010). The application of several amphibole geobarometers to the syenites, using the AMPH-IMA97 Excel Sheet (Hammarstrom and Zen 1986; Hollistaer et al. 1987; Schmidt 1992), yielded crystallization pressure estimates between 1.5 and 3.7 kbar with an average of 2.1 kbar (the uncertainty reflects both the heterogeneity in measured Al contents of amphibole and the differences among barometric calibrations). These crystallization pressures indicate a relatively shallow depth of emplacement (<10 km).

Several geothermometers were used to calculate the crystallization temperatures of the Abu Rumeil syenites. A range of two-pyroxene thermometers (Putirka 2008) yield temperatures between 894 and 1107 °C. The clinopyroxene thermometer of Lindsley (1983) is sensitive to the heterogeneity among analyzed grains and gives a wide range of crystallization temperatures, from 800 to 1100 °C (Fig 4b). These temperatures of clinopyroxene crystallization represent temperatures that existed in magma chambers or conduits well before emplacement, since petrographic observations indicate that clinopyroxene is the earliest crystallized mineral phase.

The $Fe^{2+}/(Fe^{2+} + Mg)$ ratios of the primary amphiboles of the Abu Rumeil syenites are plotted against Al^{IV} in Fig. 9. The low $Fe^{2+}/(Fe^{2+} + Mg)$ (0.31–0.45) ratios indicate strikingly high oxygen fugacity conditions (Anderson and Smith 1995).

Evidence of fractional crystallization and accumulation

The geochemical characteristics of Abu Rumeil syenites mostly support their evolution from a parental magma by fractional crystallization accompanied by minor contamination. On Rb vs. K_2O/Rb plots (Fig. 8b), the studied syenites exhibit a single compositional trend suggestive of derivation from a common parental magma. The general trends on variation diagrams of major oxides and some trace elements (Figs. 5 and 6) are broadly consistent with fractional crystallization and help to identify the important controlling phases. The decreases in CaO, MgO, FeO, TiO_2, and P_2O_5 with increasing SiO_2 indicate significant roles for pyroxene, amphibole, plagioclase, apatite, and magnetite and/or ilmenite. The role of feldspar fractionation is indicated by covariation on plots of Sr vs. Ba and Rb/Sr vs. Rb/Ba (Figs. 8 c, d), with decreasing Sr and Ba implying plagioclase fractionation during magmatic evolution. Increasing Rb/Ba ratios are especially indicative of alkali feldspar fractionation (Henderson 1982). Decreasing Fe_2O_3 and MgO with

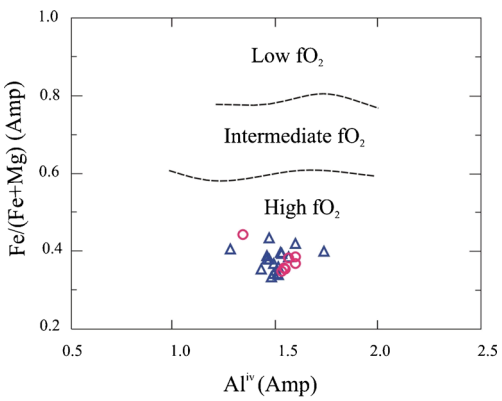

Fig. 9 $Fe^{2+}/(Fe^{2+} + Mg)$ vs. Al^{IV} diagram of the primary amphiboles (Anderson and Smith 1995). *Symbols* are as in Fig. 3

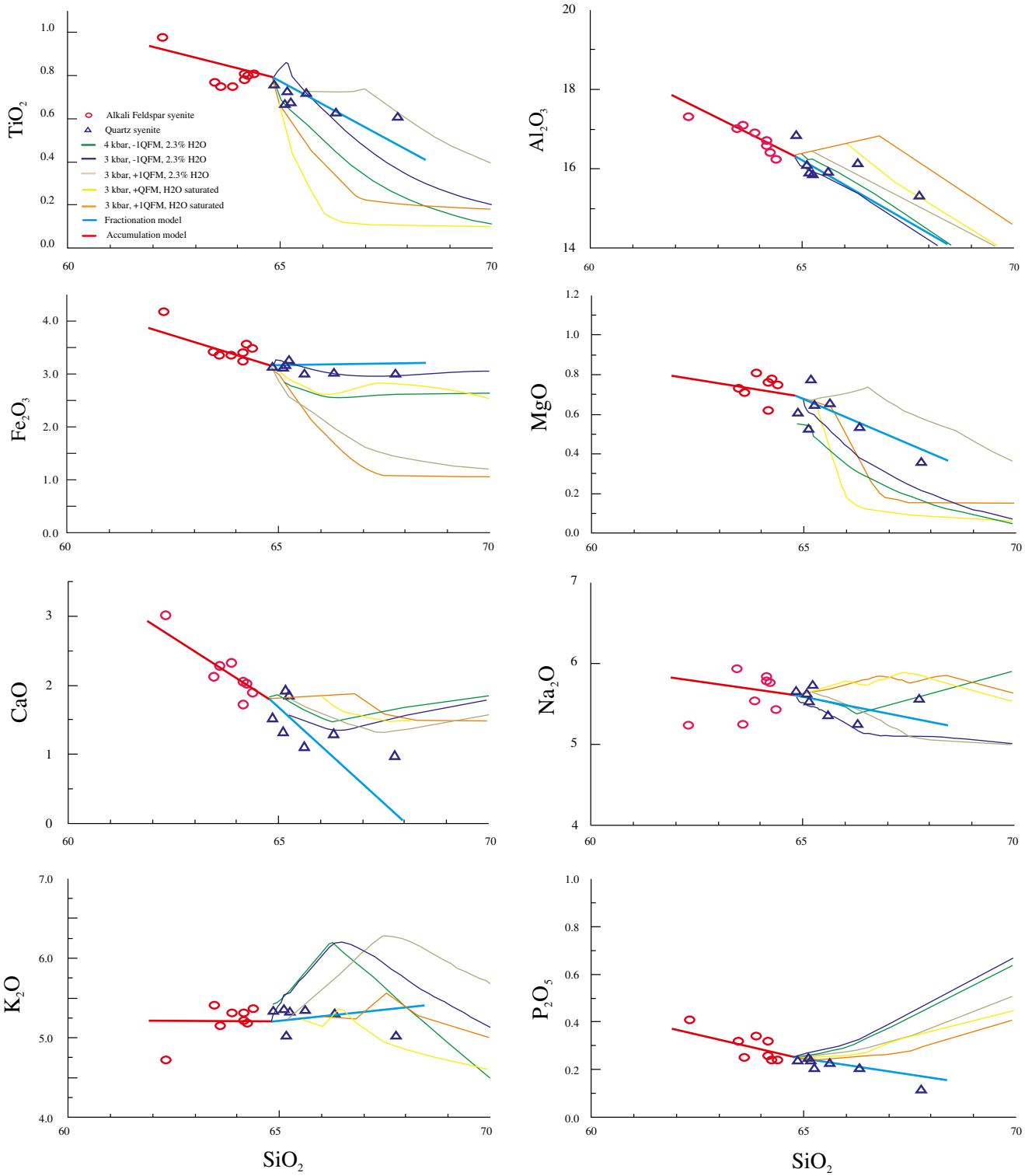

Fig. 10 Differentiation model for the Abu Rumeil syenites using major oxides. *Symbols* are as in Fig. 3

increasing SiO_2 (Fig. 5) suggests fractionation of primary mafic minerals as well. MgO vs. Rb/Sr and TiO_2 vs. Rb/Sr variation diagrams (Figs. 8 e, f) suggest fractionation of amphibole, pyroxene, and Fe-Ti oxides. The increasingly sodic plagioclase and iron-rich clinopyroxene in the quartz syenites compared to alkali feldspar syenites is consistent with ongoing fractional crystallization to reach the higher SiO_2 members of the suite (Shellnutt et al. 2016).

The opposite signs of the Eu anomalies in the alkali feldspar syenites and the quartz syenites, however, point to a

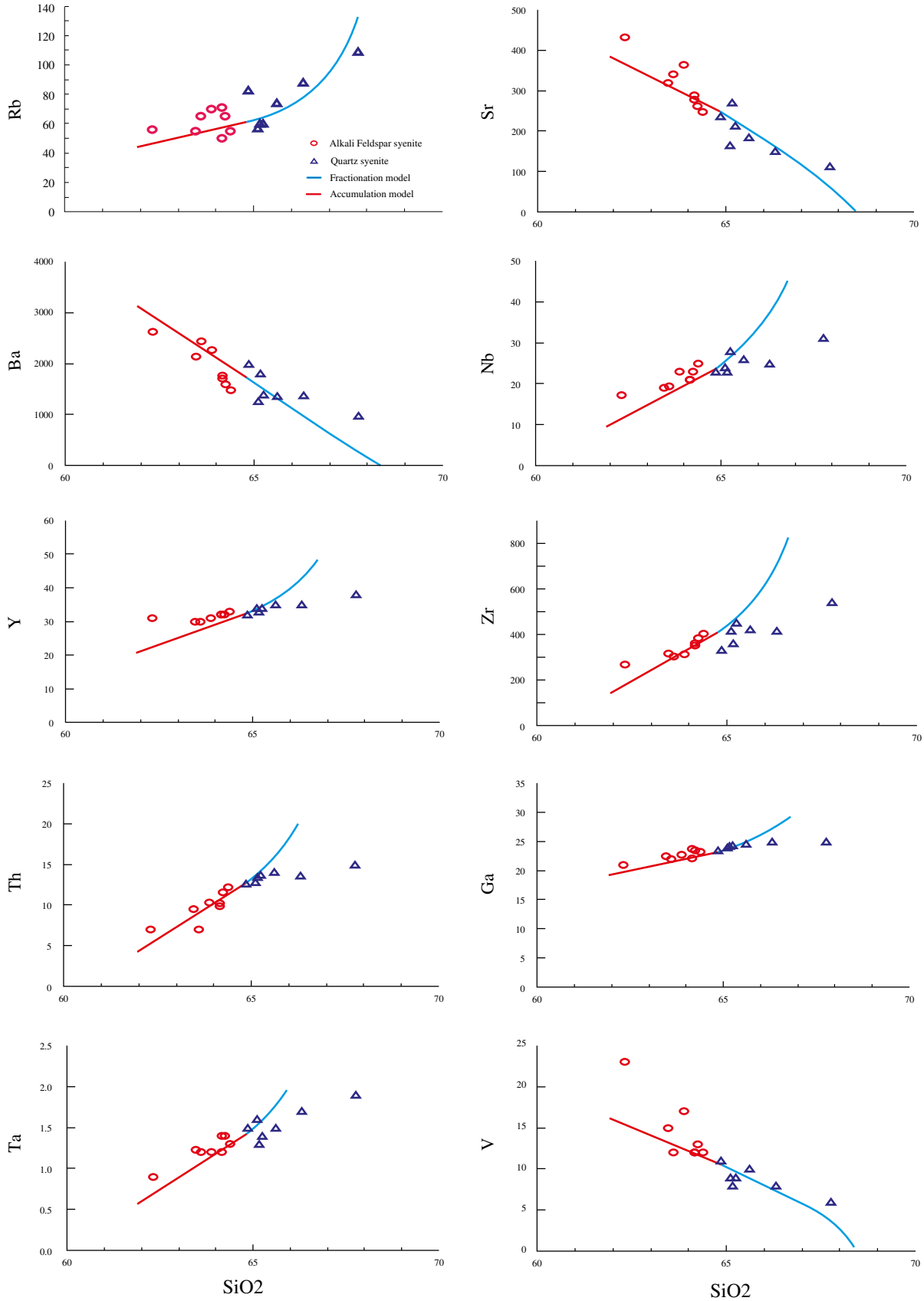

Fig. 11 Differentiation model for the Abu Rumeil syenites using trace elements. *Symbols* are as in Fig. 3

problem with a simple fractional crystallization model for the entire suite. In fact, there are subtle changes in slope at 65 % SiO_2 on most of the major and trace element variation diagrams that imply that different processes may be responsible for the compositional variations within the two rock types. Unless the parental magma inherited a strongly positive Eu anomaly, the REE patterns require that the alkali feldspar syenites were generated by crystal accumulation whereas the quartz syenites represent a liquid line of descent generated by crystal fractionation. We attempt to develop a quantitative model of these dual processes by starting with a liquid plotting between the two suites, at about 64.8 % SiO_2 and lacking a Eu anomaly. Evidently, a liquid with 64.8 % SiO_2 is not a primary mantle-derived melt; considerable differentiation and possible assimilation will already have affected it. In the absence of mafic members of the suite, however, modeling of the earlier history of evolution is a poorly constrained exercise. We therefore restrict our attention to the relationships among the collected samples.

We computed the liquidus minerals of our selected starting liquid with the rhyolite MELTS model (Gualda et al. 2012) and then subtracted an assemblage of these minerals to simulate the quartz syenite trend while adding a slightly different assemblage of these minerals to simulate the alkali feldspar syenite trend. Trace element partition coefficients for each mineral are based on McKenzie and O'Nions (1991, 1995). We were guided by the pressure, temperature, and oxygen fugacity inferences discussed above in our search for crystallization conditions that produce an optimal fit. However, finding a set of conditions where the selected primary liquid is multiply saturated with the full assemblage of plagioclase, alkali feldspar, ilmenite, pyroxene, and amphibole proved impossible. Most conditions lead to one mineral or another being first on the liquidus, which gives an interval where the liquid line of descent has the wrong slope in one or more variation diagrams. Some such simulations are shown in Fig. 10; water-saturated conditions have ilmenite or magnetite on the liquidus and TiO_2 or Fe_2O_3 decrease too quickly, whereas most conditions with lower water activity have plagioclase on the liquidus and K_2O increases too much before alkali feldspar appears. Hence, the model shown here is a generalization from the rhyolite-MELTS results rather than a single simulation run.

We selected the compositions at the first appearance of each phase on the liquidus at 3 kbar, oxygen fugacity one log unit above the QFM buffer, and with 2.3 wt.% H_2O in the initial liquid. The liquidus temperature of 978 °C is consistent with the thermometry results above. Given these mineral compositions, fractionation of an assemblage of 50 % alkali feldspar, 38.5 % plagioclase, 6 % clinopyroxene, 1 % apatite, 1 % ilmenite, and 0.35 % Ti-magnetite matches reasonably well the slope of the quartz syenite data in all the major and trace element variation diagrams (Figs. 5 and 6). The model predicts that some of the incompatible elements (Zr, Y, Nb, Th, Ta) become too enriched, compared to the evolved quartz syenites, after extensive fractionation, which may be attributed to imperfect fractional crystallization or to the appearance of unmodeled accessory phases such as zircon and monazite. The compatible behavior of V during fractionation is consistent with the oxidizing conditions selected. The selected fractionating assemblage generates a negative Eu anomaly of suitable magnitude and an overall flattening of the REE pattern (decreasing La/Yb) with progressive fractionation.

On the other hand, assimilation of 45 % alkali feldspar, 43 % plagioclase, 8 % clinopyroxene, 0.8 % apatite, 1.8 % ilmenite, and 1.5 % Ti-magnetite reproduces the major and trace element trends of the alkali feldspar syenites, including the increasing positive Eu anomaly and steeper REE patterns with decreasing SiO_2. These phase proportions are broadly similar to those that appear in the rhyolite-MELTS simulations, but were tuned within the uncertainties of the calculations in order to best fit the data.

Although amphibole, biotite, quartz, and orthopyroxene appear late in the fractionation trends, they are not necessary to explain the whole-rock chemical variations and it is likely that these phases appeared so late in the crystallization of the quartz syenites that they crystallized in situ without a fractional effect on the bulk compositional evolution of the rock suite. The differentiation model shown in Figs. 10 and 11 is not unique, but it is thermodynamically and geologically plausible and it explains the bulk of the data. We put it forward as a representative example.

Acknowledgments Special thanks are paid to King Saud University, Deanship of Scientific Research, Research Group No. RG-1436-036 for their support. We are indebted to the Geological Sciences Department, National Research Centre, Egypt, for field work assistance. M.A.'s visit to the Division of Geological and Planetary Sciences, California Institute of Technology, USA, was supported by the Cairo Initiative of the US Agency for International Development. Special thanks are given to George Rossman and Michael Baker of Caltech for allowing sample preparation facilities. Our appreciation extends to Minghua Ren (University of Nevada, Las Vegas, USA) and Chi Ma (Caltech) for their help in the microprobe analyses. Special thanks are paid to an anonymous reviewer for constructive comments as well as Editor-in-Chief Abdullah Al-Amri for valuable comments and editorial handling.

References

Abdel Khalek ML, Abdel Maksoud MA, Abdel Tawab MA, Oweiss KA (1994) Geochemistry of the St. Catherine basement rocks, Sinai, Egypt. Sci J Qatar Univ 14:134–145

Abdel Maksoud MA, Abdel Khalek ML, Oweiss KA (1993) Geologic setting of the St. Catherine basement rocks, Sinai, Egypt. Sci J Qatar Univ 13:308–318

Abdel-Rahman AM (1994) Nature of biotites from alkaline, calc-alkaline and peraluminous magmas. J Petro 35:525–541

Abdel-Rahmen AM (2006) Petrogenesis of anorogenic peralkaline granitic complexes from eastern Egypt. Mineral Mag 70:27–50

Ali BH, Wilde SA, Gabr MMA (2009) Granitoid evolution in Sinai, Egypt, based on precise SHRIMP U-Pb zircon geochronology. Gondwana Res 15:38–48

Allen CM, Chappell BW (1992) Association of I-type granites with rift-related alkaline magmatism in Central Coastal Queensland, Australia. Geol Soc Am, Abst Progress 24/7 p. 43

Anderson JL, Smith DR (1995) The effects of temperature and $fO2$ on the Al-in-hornblende barometer. Am Mineral 80:549–559

Azer MK (2006) The petrogenesis of late Precambrian felsic alkaline magmatism in South Sinai, Egypt. Acta Geol Polonica 56:463–484

Azer MK (2007) Tectonic significance of Late Precambrian calc-alkaline and alkaline magmatism in Saint Katherine area, South Sinai, Egypt. Geol Acta 5(3):255–272

Azer MK (2013) Late Ediacaran (605-580 Ma) post-collisional alkaline magmatism in the Arabian–Nubian Shield: a case study of Serbal ring-shaped intrusion, southern Sinai, Egypt. J Asian Earth Sci 77: 203–223

Azer MK, Abu El-Ela FF, Ren M (2012) The petrogenesis of late Neoproterozoic mafic dyke-like intrusion in south Sinai, Egypt. J Asian Earth Sci 54:91–109

Azer MK, El-Gharbawy RI (2011) Contribution to the Neoproterozoic layered mafic-ultramafic intrusion of Gabal Imleih, south Sinai, Egypt: implication of post-collisional magmatism in the north Arabian-Nubian Shield. J Afr Earth Sci 60:253–272

Azer MK, Obeid MA, Ren M (2014) Geochemistry and petrogenesis of late Ediacaran (580-605 Ma) post-collisional alkaline rocks from Katherina Ring complex, south Sinai., Egypt. J Asian Earth Sci 93:229–252

Azer MK, Stern RJ, Kimura J-I (2010) Origin of a Late Neoproterozoic (605±13 Ma) intrusive carbonate-albitite complex in Southern Sinai, Egypt. Int J Earth Sci 99:245–267

Be'eri-Shlevin Y, Katzir Y, Whitehouse M (2009) Post-collisional tectono-magmatic evolution in the northern Arabian-Nubian Shield (ANS): time constraints from ion-probe U-Pb dating of zircon. J Geol Soc London 166:71–85

Be'eri-Shlevin Y, Samuel MD, Azer MK, Rämö OT, Whitehouse MJ, Moussa HE (2011) The late Neoproterozoic Ferani and Rutig volcano-sedimentary successions of the northernmost Arabian-Nubian Shield (ANS): new insights from zircon U-Pb geochronology, geochemistry and O-Nd isotope ratios. Precambrian Res 188: 21–44

Bea F, Abu-Anbar M, Montero P, Peres P, Talavera C (2009) The ~844 Ma Moneiga quartz-diorites of the Sinai, Egypt: evidence for Andean-type arc or rift-related magmatism in the Arabian-Nubian Shield? Precambrian Res 175:161–168

Bentor YK (1985) The crustal evolution of the Arabo-Nubian Massif with special reference to Sinai Peninsula. Precambrian Res 28:1–74

Beyth M, Stern RJ, Altherr R, Kröner A (1994) The late Precambrian Timna igneous complex Southern Israel: evidence for comagmatic-type sanukitoid monzodiorite and alkali granite magma. Lithos 31: 103–124

Black R, Lameyre J, Bonin B (1985) The structural setting of alkaline complexes. J Afr Earth Sci 3:5–16

Blundy TD, Holland JJB (1990) Calcic amphibole equilibria and a new amphibole-plagioclase geothermometer. Contrib Mineral Petrol 104:208–224

Bonin B (2007) A-type granites and related rocks: evolution of a concept, problems and prospects. Lithos 97:1–29

Clemens JD, Holloway JR, White AJR (1986) Origin of an A-type granites: experimental constraints. Am Mineral 71:317–324

Conceição RV, Green DH (2004) Derivation of potassic (shoshonitic) magmas by decompression melting of phlogopite-pargasite lherzolite. Lithos 72:209–229

Creaser RA, Price RC, Wormald RJ (1991) A-type granites revisited: assessment of a residual-source model. Geology 19:163–166

Currie KL (1989) New ideas on an old problem: the peralkaline rocks. Geol Soc India Mem 15:117–136

Deer WA, Howie RA, Zussman J (1992) An introduction to the rock forming minerals. Longman Scientific and Technical, London

Eyal M, Litvinovsky B, Jahn BM, Zanvilevich A, Katzir Y (2010) Origin and evolution of post-collisional magmatism: coeval Neoproterozoic calc-alkaline and alkaline suites of the Sinai Peninsula. Chem Geol 269:153–179

Eyal M, Zanvilevich AN, Litvinovsky BA, Jahn BM, Vapnik Y, Be'eri-Shlevin Y (2014) The Katherina ring complex (Sinai Peninsula, Egypt): sequence of emplacement and petrogenesis. Am J Sci 314: 462–507

Farahat ES, Azer MK (2011) Post-collisional magmatism in the northern Arabian-Nubian Shield: the geotectonic evolution of the alkaline suite at G. Tarbush area, south Sinai, Egypt. Chemie der Erde 71: 247–266

Farahat ES, Mohamed HA, Ahmed AF, El Mahallawi MM (2007) Origin of I- and A-type granitoids from the Eastern Desert of Egypt: implications for crustal growth in the northern Arabian-Nubian Shield. J Afr Earth Sci 49:43–58

Friz-Töpfer A (1991) Geochemical characterization of Pan-African dyke swarms in southern Sinai: from continental margin to intraplate magmatism. Precambrian Res 49:281–300

Frost BR, Barnes CG, Collins WJ, Arculus RJ, Ellis DJ, Frost CD (2001) A geochemical classification for granitic rocks. J Petrol 42:2033–2048

Garfunkel Z (1999) History and paleogeography during the Pan-African orogen to stable platform transition: reappraisal of the evidence from the Elat area and the northern Arabian-Nubian Shield. Israel J Earth Sci 48:135–157

Gualda GAR, Ghiorso MS, Lemons RV, Carley TL (2012) Rhyolite-MELTS: a modified calibration of MELTS optimized for silica-rich, fluid-bearing magmatic systems. J Petrol 53(5):875–890

Hammarstrom JM, Zen E-A (1986) Aluminium in hornblende: an empirical igneous geobarometer. Am Mineral 71:1297–1313

Harris NBW (1985) Alkaline complexes from the Arabian Shield. J Afr Earth Sci 3:83–88

Hastie AR, Kerr AC, Pearce JA, Mitchell SF (2007) Classification of altered volcanic island arc rocks using immobile trace elements: development of the Th-Co discrimination diagram. J Petrol 48: 2341–2357

Henderson P (1982) Inorganic geochemistry. Pergamon Press, Oxford

Hollistaer LS, Grissom GC, Peters EK, Stowell HH, Sisson VB (1987) Confirmation of the empirical correlation of Al in hornblende with pressure of solidification of calc-alkaline plutons. Am Mineral 72: 231–239

Jahn BM, Litvinovsky BA, Zanvilevich AN, Reichow M (2009) Peralkaline granitoid magmatism in the Mongolian–Transbaikalian Belt: evolution, petrogenesis and tectonic significance. Lithos 113: 521–539

Jarrar GH, Manton WI, Stern RJ, Zachmann F (2008) Late Neoproterozoic A-type granites in the northernmost Arabian-Nubian Shield formed by fractionation of basaltic melts. Chemie der Erde 68:295–312

Jung S, Hoffer E, Hoernes S (2007) Neoproterozoic rift-related syenites (Northern Damara Belt, Namibia): geochemical and Nd-Sr-Pb-O isotope constraints for mantle sources and petrogenesis. Lithos 96: 415–435

Katzir Y, Eyal M, Litvinovsky BA, Jahn BM, Zanilevich AN, Valley JW, Beeri Y, Shimshilashvili E (2007) Petrogenesis of A-type granites

and origin of vertical zoning in the Katharina pluton, Gebel Mussa (Mt. Moses) area, Sinai, Egypt. Lithos 95:208–228

Kay RW, Mahlburg-Kay S (1991) Creation and destruction of lower continental crust. Geolo Rundsch 80(2):259–278

Kessel R, Stein M, Navon O (1998) Petrogenesis of late Neoproterozoic dikes in the northern Arabian-Nubian Shield: implications for the Origin of A-type granites. Precambrian Res 92:195–213

Khalil AES, Obeid MA, Azer MK (2015) Late Neoproterozoic post-collisional mafic magmatism in the Arabian–Nubian Shield: a case study from Wadi El-Mahash gabbroic intrusion in southeast Sinai, Egypt. J Afr Earth Sci 105:29–46

King PL, White AJR, Chappel BW, Allen CM (1997) Characterization and origin of aluminous A-type granites from the Lachlan Fold Belt, southeastern Australia. J Petrol 38:371–391

Lameyre J, Bowden P (1982) Plutonic rock type series: discrimination of various granitoids series and related rocks. J Volcanol Geoth Res 14: 169–186

Le Bas MJ, Le Maitre RW, Streckeisen A, Zanetin B (1986) A chemical classification of volcanic rocks based on the total alkali–silica diagram. J Petrol 27:745–750

Le Maitre RW (2002) Igneous rocks. A classification and glossary of terms. Recommendations of the International Union of Geological Sciences Subcommission on the Systematics of Igneous Rocks. Cambridge, New York

Leake BE (1997) Nomenclature of amphiboles: report of the Subcommittee on Amphiboles of the International Mineralogical Association Commission on New Minerals and Mineral Names. Mineral Mag 61:295–321

Leat PT, Thompson RN, Morrison MA, Hendry GL (1998) Silicic magma derived by fractional-crystallization from Miocene minette, Elkhead Mountain, Colorado. Mineral Mag 52:577–585

Liégeois JP, Navez J, Black R, Hertogen J (1998) Contrasting origin of post-collision high-K calc-alkaline and shoshonitic versus alkaline and peralkaline granitoids. The use of sliding normalization. Lithos 45:1–28

Lindsley DH (1983) Pyroxene thermometry. Am Mineral 64:477–493

Litvinovsky BA, Jahn BM, Eyal M (2015) Mantle-derived sources of syenites from the A-type igneous suites—new approach to the provenance of alkaline silicic magmas. Lithos 232:242–265

Litvinovsky BA, Jahn BM, Zanvilevich AN, Saunders A, Poulain S (2002) Petrogenesis of syenite–granite suites from the Bryansky Complex (Transbaikalia, Russia): implications for the origin of A-type granitoid magmas. Chem Geol 189:105–133

Litvinovsky BA, Tsygankov AA, Jahn BM, Katzir Y, Be'eri-Shlevin Y (2011) Origin and evolution of overlapping calc-alkaline and alkaline magmas: the Late Palaeozoic postcollisional igneous p0rovince of Transbaikalia (Russia). Lithos 125:845–874

Litvinovsky BA, Zanvilevich AN, Wickham SM, Steele IM (1999) Origin of syenite magmas in A-type granitoid series: syenite–granite series fromTransbaikalia. Petrology 7:483–508

Lubala RT, Frick C, Roders JH, Walraven F (1994) Petrogenesis of syenites and granites of the Schiel Alkaline Complex, Northern Transvaal, Southern Africa. J Geol 102:307–309

McKenzie D, O'Nions RK (1995) The source regions of ocean island basalts. J Petrol 36:133–159

McKenzie D, Onions RK (1991) Partial melt distributions from inversion of rare-earth element concentrations. J Petrol 32(5):1021–1091

Menuge JF, Brewer TS, Seeger CM (2002) Petrogenesis of metaluminous A-type rhyolites from the St. Francois Mountains, Missouri and the Mesoproterozoic evolution of the southern Laurentian margin. Precambrian Res 113:269–291

Mingram B, Trumbull RB, Littman S, Gerstenberger H (2000) A petrogenetic study of androgenic felsic magmatism in the Cretaceous Paresis ring complex, Namibia: evidence for mixing of crust and mantle-derived components. Lithos 54:1–22

Miyashiro A (1978) Nature of alkalic rock series. Contrib Mineral Petrol 66:91–104

Miyazaki T, Kagami H, Mohan VR, Shuto K, Morikiyo T (2003) Enriched subcontinental lithospheric mantle in the northern part of the South Indian Granulite Terrain: evidence from Yelagiri and Sevattur syenite plutons, Tamil Nadu, South India. Gondwana Res 6:585–594

Moghazi AM, Harbi HM, Ali KA (2011) Geochemistry of the Late Neoproterozoic Hadb adh Dayheen ring complex, Central Arabian Shield: implications for the origin of rare-metal-bearing post-orogenic A-type granites. J Asian Earth Sci 42:1324–1340

Montel JM, Vielzeul D (1997) Partial melting of greywackes: part II. Composition of minerals and melts. Contrib Mineral Petrol 128: 176–196

Morag N, Avigad D, Gerdes A, Belousova E, Harlavan Y (2011) Crustal evolution and recycling in the northern Arabian-Nubian Shield: new perspectives from zircon Lu–Hf and U–Pb systematics. Precambrian Res 186:101–116

Moreno JA, Molina JF, Montero P, Abu Anbar M, Scarrow JH, Cambeses A, Bea F (2014) Unraveling sources of A-type magmas in juvenile continental crust: constraints from compositionally diverse Ediacaran post-collisional granitoids in the Katerina Ring Complex, southern Sinai, Egypt. Lithos 192:56–85

Moreno JA, Montero P, Abu Anbar M, Molina JF, Scarrow JH, Talavera C, Cambeses A, Bea F (2012) SHRIMP U-Pb zircon dating of the Katerina Ring Complex: insights into the temporal sequence of Ediacaran calc-alkaline to peralkaline magmatism in southern Sinai, Egypt. Gondwana Res 21:887–900

Morimoto N, Fabries J, Ferguson AK, Ginzburg IV, Ross M, Seifert FA, Zussman J (1988) Nomenclature of pyroxenes. Mineral Mag 52: 535–550

Morrison GW (1980) Characteristics and tectonic setting of the shoshonite rock association. Lithos 13:97–108

Mushkin A, Navon O, Halicz L, Heimann A, Hartmann G, Stein M (2003) The petrogenesis of A-type magmas from the Amram Massif, southern Israel. J Petrol 44:815–832

Nesbitt HW, Young GM (1982) Early Proterozoic climates and plate motions inferred from major element chemistry of lutites. Nature 299:715–717

Nachit H, Razafimahefa N, Stussi JM, Carron JP (1985) Composition chimique des biotites et typologie magmatique des granitoides. CR Hebdomadaires Acad sci 301(11):813–818

Nachit H, Ibhi A, Abia EH, Ohoud MB (2005) Discrimination between primary magmatic biotites, reequilibrated biotites and neoformed biotites. Compt Rendus Geosci. 337:1415–1420

Patchett PJ, Chase CG (2002) Role of transform continental margins in major crustal growth episodes. Geology 30:39–42

Pearce JA (1983) Role of sub-continental lithosphere in magma genesis at active continental margins. In: Hawkesworth CJ, Norry MJ (eds) Continental basalts and mantle xenoliths. Shiva Pub, UK, pp. 230–240

Pearce JA (1996) Sources and settings of granitic rocks. Episodes 19: 120–125

Pearce JA, Bender JF, et al. (1990) Genesis of collision volcanism in Eastern Anatolia, Turkey. J Volcanol Geoth Res 44:189–229

Pearce JA, Harris NBW, Tindle AG (1984) Trace element discrimination diagrams for the tectonic interpretation of granitic rocks. J Petrol 25: 956–983

Putirka K (2008) Thermometers and barometers for volcanic systems. In: Putirka K, Tepley F (eds) Minerals, inclusions and volcanic processes. Am Mineral Soc, Washington DC, Rev Mineral Geochem, pp 69:61–120

Richard LR (1995) Mineralogical and petrological data processing system. Minpet Software (C):1988–1985 Version 2.02

Ridolfi F, Renzulli A, Puerini M (2010) Stability and chemical equilibrium of amphibole in calc-alkaline magmas: an overview, new

thermobarometric formulations and application to subduction-related volcanoes. Contrib Mineral Petrol 160:45–66

Rogers NW, James D, Kelley SP, DeMulder M (1998) The generation of potassic lavas from the eastern Virunga Province, Rwanda. J Petrol 39:1223–1247

Samuel MD, Moussa HE, Azer MK (2007) A-type volcanics in Central Eastern Sinai, Egypt. J Afr Earth Sci 47:203–226

Schmidt MW (1992) Amphibole composition in tonalite as a function of pressure: an experimental calibration of the Al-in hornblende barometer. Contrib Mineral Petrol 110:304–310

Shellnutt JG, Lee T-Y, Yang CC, Hu S-T, Wu J-C, Iizuka Y (2016) A mineralogical investigation of the Late Permian Doba gabbro, southern Chad: constraints on the parental magma conditions and composition. J Afr Earth Sci 114:13–20

Shellnutt JG, Zhou M-F, Zellmer GF (2009) The role of Fe–Ti oxide crystallization in the formation of A-type granitoids with implications for the Daly gap: an example from the Permian Baima igneous complex, SW China. Chem Geol 259:204–217

Stern RJ (1994) Arc assembly and continental collision in the Neoproterozoic East African Orogen: implications for the consolidation of Gondwanaland. Annu Rev Earth Pl Sc 22:319–351

Stern RJ (2002) Crustal evolution in the East African Orogen: a neodymium isotopic perspective. J Afr Earth Sci 34:109–117

Stern RJ, Gottfried D (1986) Petrogenesis of a Late Precambrian (575-600 Ma) bimodal suite in Northeast Africa. Contrib Mineral Petrol 92:492–501

Stern RJ, Voegeli DA (1987) Geochemistry, geochronology, and petrogenesis of a late Precambrian (~590 Ma) composite dike from the North Eastern Desert of Egypt. Geol Rundsch 76:325–341

Stevenson R, Upton BGJ, Steenfelt A (1997) Crust mantle interaction in the evolution of the Ilímaussaq Complex, South Greenland: Nd isotopic studies. Lithos 40:189–202

Stoeser DW, Frost CD (2006) Nd, Pb, Sr and O isotope characterization of Saudi Arabian Shield terranes. Chem Geol 226:163–188

Streckeisen A, Le Maitre RW (1979) A chemical approximation to the modal QAPF classification of igneous rocks. Neues Jb Miner Abh 136:169–206

Sun S-S, McDonough WF (1989) Chemical and isotopic systematics of oceanic basalts: implications for mantle composition and processes. In: Saunders AD, Norry MJ (eds) Magmatism in the ocean basins. Geol Soc London, pp. 42:313–345

Sutcliffe RH, Smith AR, Doherty W, Barnett RL (1990) Mantle derivation of Archean amphibole-bearing granitoid and associated mafic rocks: evidence fromthe southern Superior Province, Canada. Contrib Mineral Petrol 105:255–274

Taylor SR, McLennan S (1995) The geochemical composition of the continental crust. Rev Geophys 33:241–265

Tchameni R, Mezger K, Nsifa NE, Pouclet A (2001) Crustal origin of early Proterozoic syenites in the Congo Craton (Ntem Complex), South Cameroon. Lithos 57:23–42

Thornton CP, Tuttle OF (1960) Chemistry of igneous rocks, I.D. Differentiation Index. Am J Sci 258:664–684

Turner SP, Foden JD, Morrison RS (1992) Derivation of some A-type magmas by fractionation of basaltic magma; an example from the Padthaway Ridge, South Australia. Lithos 28:151–179

Vail JR (1989) Ring complexes and related rocks in Africa. J Afr Earth Sci 8:19–40

Vernikovsky VA, Pease VL, Vernikovskaya AE, Romanov AP, Gee DG, Travin AV (2003) First report of early Triassic A-type granite and syenite intrusions from Taimyr: product of the northern Eurasian super plume? Lithos 66:23–36

Wang Q, Li JW, Jian P, Zhao ZH, Xiong XL, Bao ZW, Xu JF, Li CF, Ma JL (2005) Alkaline syenites in eastern Cathaysia (South China): link to Permiane-Triassic transtension. Earth Planet Sc Lett 230:339–354

Whalen JB, Currie KL, Chappel BW (1987) A-type granites: geochemical characteristics, discrimination and petrogenesis. Contrib Mineral Petrol 95:407–419

Wilson M (1994) Igneous petrogenesis. Chapman & Hall, London

Wyborn D (1992) The tectonic significance 496 of Ordovician magmatism in the eastern Lachlan Fold Belt. Tectonophysics 214: 177–192

Yang JH, Chung SL, Wilde SA, Wu FY, Chu MF, Lo CH, Fan HR (2005) Petrogenesis of post-orogenic syenites in the Sulu Orogenic Belt, East China: geochronological, geochemical and Nd–Sr isotopic evidence. Chem Geol 214:99–125

Ying JF, Zhang HF, Sun M, Tang YJ, Zhou XH, Liu XM (2007) Petrology and geochemistry of Zijinshan alkaline intrusive complex in Shanxi Province, western North China Craton: implication for magma mixing of different sources in an extensional regime. Lithos 98:45–66

Zhao J-X, Shiraishi K, Ellis DJ, Sheraton JW (1995) Geochemical and isotopic studies of syenites from the Yamoto Mountains East Antartica: implication for the origin of syenitic magmas. Geochim Cosmochim Ac 59:1363–1385